

The Development of A New Pixel Pad Detector

Dong Gan

Physics Department

McGill University, Montreal

A thesis submitted to the Faculty
of Graduate Studies and Research
in partial fulfilment of the requirements
of the Degree of Master of Science.

July, 1996

©Dong Gan, 1996



National Library
of Canada

Acquisitions and
Bibliographic Services Branch

395 Wellington Street
Ottawa, Ontario
K1A 0N4

Bibliothèque nationale
du Canada

Direction des acquisitions et
des services bibliographiques

395, rue Wellington
Ottawa (Ontario)
K1A 0N4

Your file - Votre référence

Our file - Notre référence

The author has granted an irrevocable non-exclusive licence allowing the National Library of Canada to reproduce, loan, distribute or sell copies of his/her thesis by any means and in any form or format, making this thesis available to interested persons.

L'auteur a accordé une licence irrévocable et non exclusive permettant à la Bibliothèque nationale du Canada de reproduire, prêter, distribuer ou vendre des copies de sa thèse de quelque manière et sous quelque forme que ce soit pour mettre des exemplaires de cette thèse à la disposition des personnes intéressées.

The author retains ownership of the copyright in his/her thesis. Neither the thesis nor substantial extracts from it may be printed or otherwise reproduced without his/her permission.

L'auteur conserve la propriété du droit d'auteur qui protège sa thèse. Ni la thèse ni des extraits substantiels de celle-ci ne doivent être imprimés ou autrement reproduits sans son autorisation.

ISBN 0-612-19813-8

Canada

Abstract

This research is conducted as a R&D work for the PHENIX experiment of the relativistic heavy ion collider (RHIC) at Brookhaven National Laboratory (BNL), in an effort to develop a multi-wire proportional chamber (MWPC) using a new pixel cathode pad readout method. The pads are formed by linking the pixels in a special pattern and the image charge signals on the pads are read by highly integrated CMOS digital electronic chips with chip-on-board (COB) technology. Two prototype pixel pad chambers, PC1 and PC3, were designed and constructed. The chambers were tested with high energy particle beams at BNL. This work demonstrates the feasibility and affordability of constructing and operating the pixel pad chambers with large number of channels, using the technology adopted here. Good spatial resolutions equal to about one-half the cell dimensions both ~~along and~~ perpendicular to the wire direction ($4mm$ for PC1 and $8mm$ for PC3) have been achieved. Charged particle track reconstruction efficiency and other chamber characteristics are also discussed.

Résumé

Ce travail s'inscrit dans le cadre d'un effort de recherche et développement conduit pour l'expérience PHENIX au collisionneur d'ions lourds relativistes (RHIC) du Laboratoire National de Brookhaven, dans le but de développer une chambre proportionnelle à fils multiples (MWPC) utilisant une nouvelle technologie de lecture de cathode à segmentation en pixel. Les segments sont constitués de pixels inter-reliés en un patron spécial et les signaux d'image induite sur les pixels sont lues par un système d'électronique digitale CMOS hautement intégrée avec la technologie de puce-sur-circuit (COB). Deux prototypes de chambre à segmentation en pixel, PC1 et PC3, ont été conçus et assemblés. Les chambres ont été testées à l'aide de faisceaux de particules de hautes énergies au BNL. Ce travail a démontré qu'il était possible de construire et d'opérer économiquement une chambre à pixel ayant un grand nombre de canaux en utilisant la technologie de puces hautement intégrée CMOS ainsi que la technologie COB. Une bonne résolution spatiale égale à environ la moitié de la grosseur d'une cellule dans les deux directions, perpendiculaire et parallèle à celle des fils (4mm pour PC1 et 8mm pour PC3) a été obtenue. L'efficacité de reconstruction de trajectoire de particule chargée et autres caractéristiques sont également discutées.

Acknowledgment

First of all, I would like to express my sincere thanks to Professor Tommy Mark, my supervisor. I benefit so much from his great knowledge and expertise, as well as his personality.

Special thanks to Professor Jean Barrette, who, can always give invaluable theoretical guidance throughout this work. It is always a great pleasure to discuss physics with him.

I would also like to thank Dr. Nick Starinsky. The most practical training and guidance to build these chambers were all from him.

Numerous thanks to Yujin Qi, our fellow Ph.D. student. So many puzzles were solved after discussion with him. His participation was so essential. Also lots thanks to Kirill Filimonov, who gave me great assistance in the data analyses.

Also thanks to our technician, Suzanne Abcarius, who participated all the work to build these chambers. It is always a pleasure to work together with her.

Much thanks to Professor A. Oskarsson, and T. Svensson, from Lund University, for their great contribution to this work.

Lot of thanks to Li Zhou, visiting scholar from IHEP, Beijing, China, and Dr. Fuhu Liu, for all their great assistance.

Special thanks to Dr. Ian Atatekin, who gave so much valuable assistance during the course of AutoCad design. Thanks to Dr. Leo Nikkinen, whose expertise in electronics made the electronic part of this work so much easier and enjoyable.

So much machining work was completed under the guidance of our machinists Steve Kecani and John Egyed. They deserve my sincere thanks.

I also want to thank for Roger Lacasse and Yi Dai who always gave their great advice for me.

During my two years study here in McGill University, I received many financial support which I really appreciated a lot. In 1994, part of my fellowship I received were from Professor Carl Reinhardt, and part of it were from the Natural Sciences and Engineering Research Council (NSERC). I also received the Dow Hickson Fellowship, donated by Professor Dow Hickson. Without these support, this work would have been impossible.

Finally, I want to thank my family: my parents, my sisters, for their great love and support, without whom, nothing would be possible here.

To my parents, to my sisters.

Contents

1	Introduction	1
1.1	Background	1
1.2	Scope of This Thesis	9
2	Review of The Principles of Operation of a MWPC	10
2.1	Energy Loss Mechanism	10
2.2	Ionization of Gas, Anode Avalanche	12
2.3	Induced Charge on Electrodes	15
2.4	Pad Chamber With Geometrical Charge Division	17
3	The New Pixel Pad Chamber	21
3.1	Principles of Operation of Pixel Pad Chamber	21
3.2	Measures of Detector Performance	25
3.2.1	Position Identification	25
3.2.2	Position Resolution	26
3.2.3	Position Linearity	27

4	Detector Construction	29
4.1	Design and Fabrication of Pixel Pad Chamber	30
4.1.1	Pixel Pad Chamber Design Consideration	30
4.1.2	The Pixel Cathode Board Design	33
4.1.3	The Motherboard Design	35
4.1.4	Chamber Assembly	41
4.2	Detector Electronics	43
4.2.1	Readout Card	44
4.2.2	Timing Logic	45
5	In-beam Tests	52
5.1	Experiment Setup	52
5.2	Detector Characteristics	55
5.2.1	Noise Study	55
5.2.2	Cluster Characteristics	56
5.2.3	Position Resolution	59
5.2.4	Position Linearity	60
5.2.5	Reconstruction Efficiency	61
5.2.6	High Voltage and Threshold Effects	62
6	Conclusions	81
6.1	Summary and Conclusions	81

6.2 Future Improvement	84
----------------------------------	----

List of Figures

1.1	Overview of PHENIX Detector System.	5
1.2	Structure of A Typical MWPC.	8
2.1	Electric field lines (solid line) and equi-time lines (dashed line) in PC1.	13
2.2	Equi-potential lines in PC1.	14
2.3	Pad Chamber Geometry Illustration.	15
2.4	Examples of the Chevron Pad Pattern.	18
3.1	Overview of the Pixel Pad Chamber Structure.	22
3.2	Pixel Pad Geometry Pattern.	23
3.3	Front-End Electronic Readout for Pixel Pad Chamber.	25
3.4	Cluster Classification.	26
4.1	The Basic Readout Unit.	33
4.2	FEE Readout Channel Numbering on Connector Pins, viewed from the top side of the pixel cathode board.	35

4.3	FEE Readout Channel Numbering on Pads, viewed from the top side of the pixel cathode board.	36
4.4	PC1 Pixel Cathode Board Design.	37
4.5	PC3 Pixel Cathode Board Design.	38
4.6	PC1 Motherboard Design.	39
4.7	PC3 Motherboard Design.	40
4.8	Cross Sectional View of the Mechanical Structure of the Prototype. .	41
4.9	PC1 Pixel Cathode Panel FR4 Frame.	47
4.10	PC3 Pixel Cathode Panel FR4 Frame.	48
4.11	PC1&PC3 Solid Cathode Panel FR4 Frame.	49
4.12	FEE of Readout Card Logic Structure.	50
4.13	DMU Function Description in Timing Sequence.	51
5.1	Beam Line Setup (See text for details).	53
5.2	Photograph of PC1 in Beamline.	54
5.3	Logic Diagram for the In-beam DAQ System.	63
5.4	PC1 Hits Pattern. (a) PC1 Pads Hits Pattern; (b) PC1 Cells Hits Pattern.	64
5.5	PC3 Hits Pattern. (a) PC3 Pads Hits Pattern; (b) PC3 Cells Hits Pattern.	65
5.6	PC1 Hits Distribution. (a) PC1 Pads Fired; (b) PC1 Cells Fired; (c) PC1 Clusters Fired.	66

5.7	PC3 Hits Distribution. (a) PC3 Pads Fired; (b) PC3 Cells Fired; (c) PC3 Clusters Fired.	67
5.8	PC1 Raw Data for the Reconstructed Position. (a) Reconstructed Position Along the Wires; (b) Reconstructed Position Across the Wires.	68
5.9	PC3 Raw Data for the Reconstructed Position. (a) Reconstructed Position Along the Wires; (b) Reconstructed Position Across the Wires.	69
5.10	PC1 Reconstructed Position Resolution under Any Wire. (a) Reconstructed Position Resolution Along the Wires; (b) Reconstructed Position Resolution Across the Wires.	70
5.11	PC3 Reconstructed Position Resolution under Any Wire. (a) Reconstructed Position Resolution Along the Wires; (b) Reconstructed Position Resolution Across the Wires.	71
5.12	PC1 Reconstructed Position Resolution under One Particular Wire. (a) Reconstructed Position Resolution Along the Wires; (b) Reconstructed Position Resolution Across the Wires.	72
5.13	PC3 Reconstructed Position Resolution under One Particular Wire. (a) Reconstructed Position Resolution Along the Wires; (b) Reconstructed Position Resolution Across the Wires.	73
5.14	Position Linearity for PC1. (a) Non-linearity Along the Wires; (b) Global Position Resolution.	74

5.15 Position Linearity for PC3. (a) Non-linearity Along the Wires; (b)	
Global Position Resolution.	75
5.16 Basic Non-linearity Pattern.	76
5.17 PC1, Efficiency on the Total Charge.	77
5.18 PC3, Efficiency on the Total Charge.	78
5.19 (a)Fired Pads Efficiency vs. Threshold; (b)Fired Cells Efficiency vs.	
Threshold.	79
5.20 (c)Fired Pads Efficiency vs. High Voltage; (d)Fired Cells Efficiency	
vs. High Voltage	80

List of Tables

4.1	Pixel Pad Parameters	30
4.2	Pixel Pad Chamber Parameters	32
5.1	Noise Study for PC3.	56
5.2	Fired Cells Category, $HV = 1750V$ for PC1, $HV = 2200V$ for PC3 ..	58
5.3	Fired Clusters Classification.	59
5.4	Best Measured Position Resolution.	60

Chapter 1

Introduction

1.1 Background

The puzzles of symmetry breaking and unseen isolated quarks are among the major problems in our modern physics. High energy heavy-ion collisions may provide a valuable tool to examine these puzzles in strongly interacting quark-gluon systems[1]. An important objective of high-energy heavy-ion collisions is to search for a new form of matter under extreme conditions of high energy densities and high temperatures. When a nucleus travels at very high speed, Lorentz contraction causes a compression of the nucleus into high baryon density. When two such nuclei approach each other, the elementary nucleon-nucleon collision between the two nuclei occur nearly at the same time and in close spatial proximity. In consequence, as the colliding baryon matter recedes from each other after the collision, a large amount of energy

is deposited in a small region of space in a short duration of time. In this region, an energy density of the order of a few GeV/fm^3 may be achieved. At this energy density, an order of magnitude greater than the energy density of normal nuclear matter, a large number of primary pions would be created out of the Fermi sea. The sudden increase in hadron density may favor the formation of new form of matter such as the quark-gluon plasma (QGP), as predicted by the quantum chromodynamic theory (QCD). It is a state of matter believed to have existed in the early evolution of the universe and may still be existing in the core of some remote neutron stars.

The critical conditions for such phase transition into QGP can be summarized as: 1) for pure lattice gauge (gluons only), the transition is first order with critical temperature $T_c \sim 200 MeV$ and energy density $\epsilon_c \sim 1 GeV/fm^3$; 2) for 2 flavors of light quarks, the transition is second order with $T_c \sim 150 MeV$; 3) for 3 flavors, the transition appears to be first order with similar T_c [2].

It is believed that QGP can be produced in the laboratory by bombarding a target nucleus with another projectile nucleus at ultra-relativistic energy. The Relativistic Heavy-Ion Collider (RHIC), which is being constructed at Brookhaven National Laboratory (BNL), is designed to accelerate colliding beams of nuclei as heavy as gold to an energy of about $100 GeV$ per nucleon per beam. In the collision of a gold nucleus with another gold nucleus in such a collider, the energy carried by each nucleus is about $100 \times 197 GeV$, or $19.7 TeV$, and the center-of-mass energy \sqrt{s} is about $2 \times 19.7 TeV$, or $39.4 TeV$. A collision volume of several hundred cubic fermis with

an energy density as high as $10\text{GeV}/fm^3$ would be created. The magnitude of energy involved in nucleus-nucleus collisions is indeed very large, more than sufficient to create an environment for a phase transition from hadronic matter to QGP.

The PHENIX experiment at RHIC at BNL is dedicated to the discovery of QGP and to measure its properties. It is being mounted by an international collaboration of some 400 physicists from 45 institutions in 10 countries. The PHENIX experiment is based on a large detector system comprising many subsystems. The PHENIX detector with all its subsystems indicated is shown in Fig. 1.1. The PHENIX strategy is to perform a systematic investigation of leptonic, photonic, and hadronic signatures and to look for a simultaneous anomaly attributable to QGP formation. Many potential signatures that identify the QGP state have been proposed over the years for experimental investigation. Some examples are:

- Photon thermal radiation enhancement.
- Dilepton production enhancement with certain invariant masses.
- ϕ , ρ , and ω production.
- Enhancement of strange particle (K, Λ , Ξ etc.) production.
- Suppression of J/ψ production.
- Pion correlation.
- Hadron transverse momentum p_T distribution.

- Transverse energy E_T production.
- Multiplicity of charged particles (N_{ch}) and their distribution in space.

The important physics topics in PHENIX experiment include deconfinement (Debye Screening), chiral symmetry restoration, thermal radiation of hot gas, nature of the phase transition, strangeness and charm production, jet quenching, and space-time evolution. Because the physics of interest involves many different kinds of particles, particle identification is very important. The PHENIX approach is to identify and measure leptons, photons, and hadrons as a function of energy density in both nucleus-nucleus, $A + A$, and nucleon-nucleus, $p + A$, collisions. According to Bjorken[3], the energy density ϵ is given by:

$$\epsilon \simeq \frac{1}{\pi c R_{\perp}^2 \tau_0} \frac{dE_T}{dy} \approx \frac{1}{\pi c R_{\perp}^2 \tau_0} \sqrt{\langle p_T^2 \rangle c^2 + m_{\pi}^2 c^4} \frac{dN_{\pi}}{dy} \quad (1.1)$$

Where dE_T/dy is the rapidity density of transverse energy E_T , $N_{\pi} = (N_{\pi^-} + N_{\pi^0} + N_{\pi^+})$ is the multiplicity of pions, R_T is the transverse radius, and τ_0 is typically estimated as $1fm/c$. As a means of fixing the collision geometry (mainly R_{\perp}), the charged particle multiplicity, $N_{ch} \simeq (N_{\pi^+} + N_{\pi^-})$, will be measured over a wide range of rapidity to eliminate possible fluctuation effects. Then, dE_T/dy , measured with an electromagnetic calorimeter for a narrow bin of rapidity, is related to ϵ at that rapidity by the above equation. By examine all measurable signatures as a function of either $dN_{\pi^{\pm}}/dy$ or dE_T/dy , we will then be able to study the variation of these

51

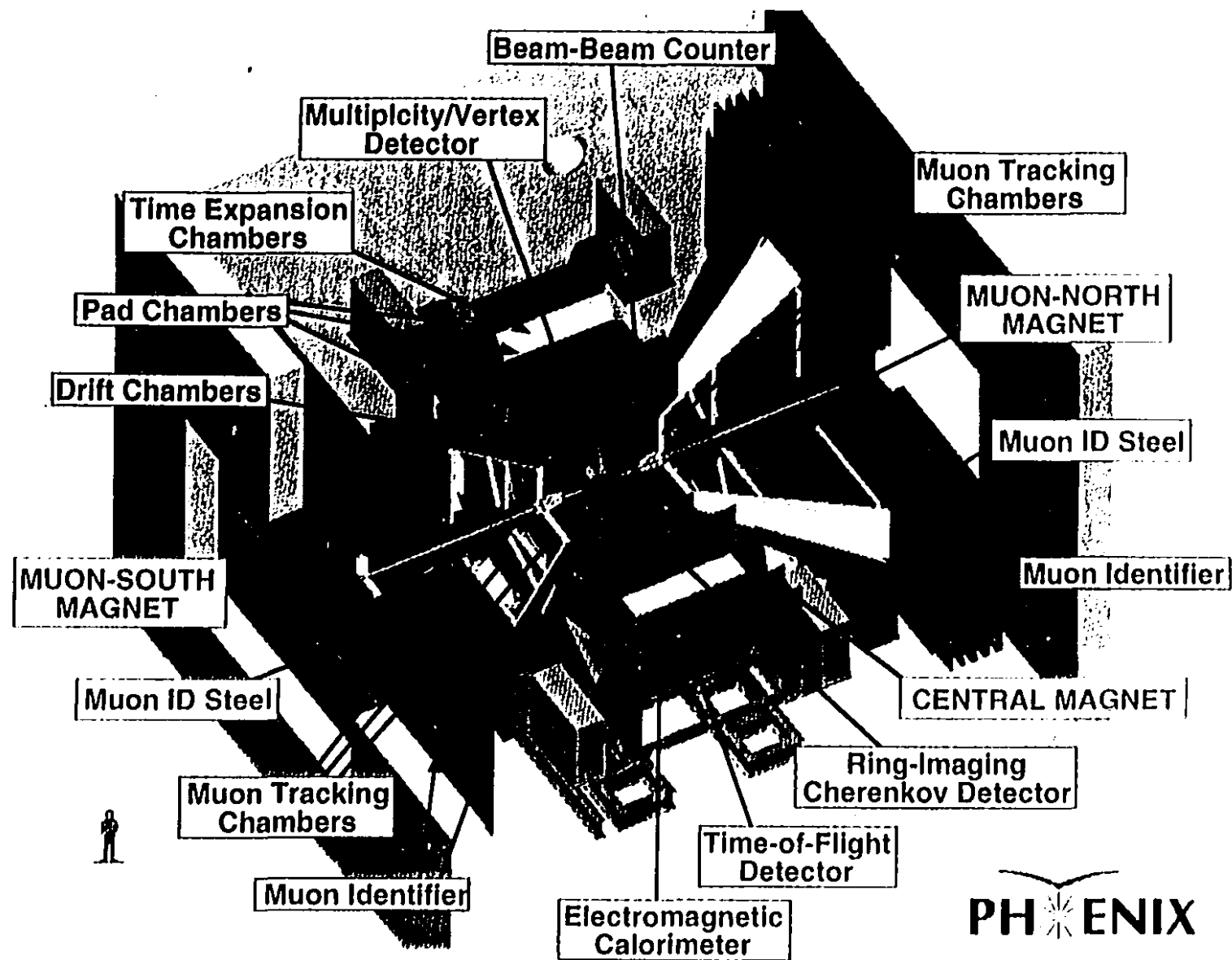


Figure 1.1: Overview of PHENIX Detector System.

signals as a function of both local (dE_T/dy) and global (dN_{\pm}/dy) estimates of the energy density.

To measure all the charged particles, the PHENIX experiment must be able to track them. The PHENIX tracking system contains three subsystems, the drift chambers (DC), the pad chambers (PC), and the time expansion chamber (TEC). The system is designed to: 1) locate all charged particle tracks of interest within their fiducial volume, 2) measure the particle momenta, 3) help to identify which of the tracks are electrons, and 4) contribute information to the trigger. The low mass, multiwire focusing drift chambers can provide high resolution p_T measurements. The three nonprojective pad chambers can provide a three-dimensional position measurements to aid in pattern recognition and to determine p_z/p_T . They can also provide three space points for a second-level trigger. A time expansion chamber assists in the pattern recognition and provides e/π separation from 5×10^{-3} at a momentum of $250 \text{ MeV}/c$ to 10^{-1} at $2.5 \text{ GeV}/c$ from energy loss (dE/dx) information.

The McGill University nuclear physics group in PHENIX is leading the effort for the development, design, construction and commissioning of the pad chamber subsystem. Part of the R&D work of this project at McGill University forms the main subject of this thesis. The pad chambers are multiwire proportional chambers (MWPC), in which a wire plane interspersed with anode and field wires is “sandwiched” by two cathodes, with one or both cathode planes divided into sensitive pads used to determine the positions of particles traversing the detector. The space

between the two cathodes are filled with appropriate gas so that the charged particles pass through the active gas volume produce ionization along their trajectories. Electrons from each track will drift to the nearest anode wire causing an avalanche to occur. The resulting charge cloud induces, by capacitive coupling, a charge distribution on the cathode pads close to the avalanche location. The schemes usually employed for the determination of the avalanche position, can be divided into three categories: resistive charge division, capacitive charge division and geometrical charge division. In the geometrical charge division method, pads of specific geometric shape are chosen to sample the charge induced on the cathode. The basic structure of a MWPC, which uses the geometrical charge division method, is given as Fig. 1.2. The wire plane alternating with the anode and field wires is symmetrically placed between the two cathodes, one upper plane and the other lower plane with geometrical pattern.

Previous R&D work for pad chamber carried out in McGill University mainly concentrated on the MWPC with chevron shaped cathode pad for geometrical charge division. According to this previous work, the chevron cathode pad chamber can offer good spatial resolution, large pad size (hence low channel count), low mass and proven reliability[4, 5, 6]. However, the construction of such chambers for detection over a large area, as required here in the PHENIX experiment is fairly demanding. The anode-cathode geometry and the pad geometry have tight tolerances too. Because of the requirement of relatively high precision analog readout electronics, the cost

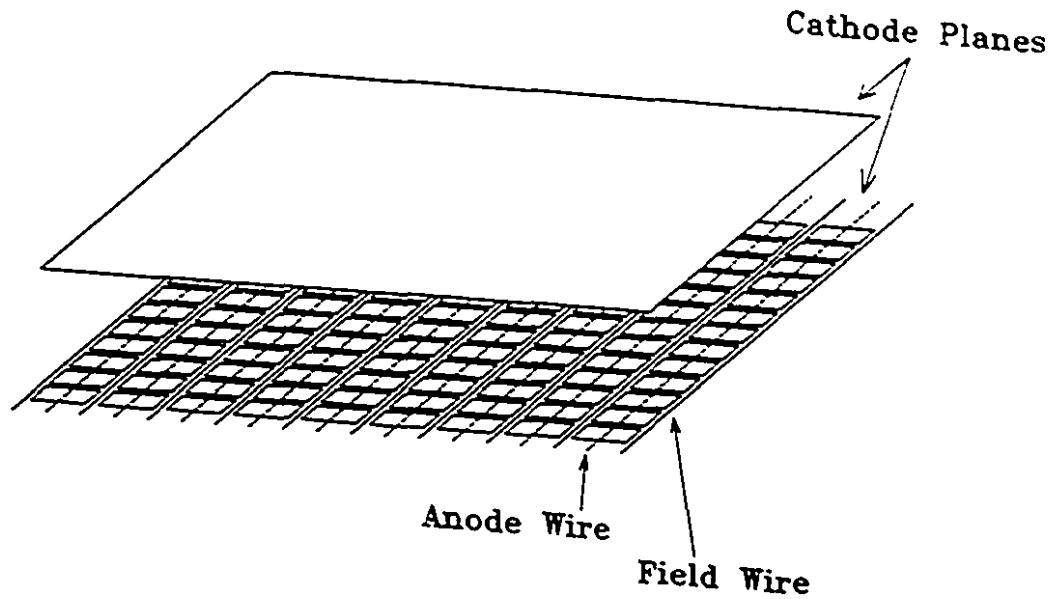


Figure 1.2: Structure of A Typical MWPC.

per channel is comparatively high, almost 40\$ per channel, which limits the channel count to a relatively low number. This necessitates the use of large pad size, making such chevron chamber less than ideal for two track resolution.

With the pixel pad cathode option, all these shortcomings can be solved. The good spatial resolution can be achieved with the choice of the pixel pad sizes to coincide with the required spatial resolution. With its digitized readout systems, the cost can be dramatically reduced to 4\$ per channel[7] which would allow the use of large number of channels. And chambers using the pixel pad design would also improve the double hit resolution.

It is under these consideration, in this thesis work, the two prototypes PC1 and PC3, which have different pixel pad sizes, were developed, to test the chambers'

performance and reliability.

1.2 Scope of This Thesis

This thesis is divided into six chapters. A review of the principles of operation of the MWPC is given in Chapter Two. Principles of operations of pixel pad chamber are discussed in Chapter Three. Chapter Four describes the design, implementation and operation of the two pixel pad chambers built. The in-beam test results for these two chambers are presented in Chapter Five. Conclusions and future improvement of these detectors are also discussed in Chapter Six.

The coordinate system used throughout this thesis is defined as follows:

- x axis is the direction along the anode wires but in the wire plane.
- y axis is the direction perpendicular to the anode wires but in the wire plane.
- z axis is the direction of the incident particle beam perpendicular to the wire plane.

Chapter 2

Review of The Principles of Operation of a MWPC

This chapter reviews the basic principles of operation of a MWPC. The mechanism by which a charged particle loses its energy in traversing a gas filled detector such as MWPC, and other basic physical processes inside a MWPC, are keys to the understanding of the operation of our pixel pad chamber.

2.1 Energy Loss Mechanism

When an energetic charged particle passes through a gas, it undergoes a series of inelastic Coulomb collisions with the electrons of the gas molecules, as well as elastic scattering from the gas nuclei. The main part of the energy loss of energetic charged particles comes from the inelastic part, as the part due to nuclear processes

is negligible compared with the former. As a result, the particle loses its energy by excitation and ionization of the gas molecules, leaving a trail of electron-ion pairs along its trajectory.

The stopping power, dE/dx , the average energy loss per unit path length by an energetic charged heavy particle, is given by the Bethe-Bloch formula[8]:

$$\frac{dE}{dx} = -\frac{4\pi N_0 z^2 e^4}{m_e c^2} \frac{Z}{A} \frac{\rho}{\beta^2} \left[\ln\left(\frac{2m_e v^2}{I(1-\beta^2)}\right) - \beta^2 \right] \quad (2.1)$$

where m_e is the electron mass, $\beta = v/c$, z and v are the charge and velocity of incident particle, N_0 is the Avogadro's number, Z , A and ρ are the atomic number, mass number and mass density of the gas atoms or molecules, I is the effective ionization potential averaged over all electrons. ($I = I_0 Z$, $I_0 \approx 10\text{eV}$ for $Z > 30$).

The following conclusions can be derived from Eq. 2.1:

1. The stopping power, dE/dx , is independent of the mass M of the incident particle.
2. The stopping power, dE/dx , depends on the velocity of the incident charged particle. It varies as $1/v^2$ at nonrelativistic velocities, reaches a minimum of $E \approx 3Mc^2$, and increases logarithmically with the slowly varying $\gamma = 1/\sqrt{1-\beta^2}$ at relativistic velocities. As a result, all single charged heavy particles having stopping power tend to have more or less the same minimum value, and they are called the minimum ionizing particles (MIP).

3. The stopping power, dE/dx , is proportional to the square of the charge of the incident particles. Therefore, the larger charge the particles carry, the quicker they loss their energy, the less power they have to pass through the gas, as long as the particles process the same velocities.

The energy loss by electron or positron passing through a gas has the similar formula. The stopping power of electron or positron, dE/dx , is given as[8]:

$$\frac{dE}{dx} = -\frac{2\pi N_0 e^4}{m_e c^2} \frac{Z}{A} \frac{\rho}{\beta^2} \left[\ln\left(\frac{m_e v^2 E}{I^2 (1 - \beta^2)}\right) - \beta^2 \right] \quad (2.2)$$

All the parameters in this equation are same as those in Eq. 2.1. It can been seen that, at the same energy, compared with heavy charged particles, electron or positron has larger velocity, the energy loss of them is less significant. Therefore, they are much easier to pass through a gas.

2.2 Ionization of Gas, Anode Avalanche

By excitation and ionization, an incident charged particle, will create a collection of electrons and positive ions along its trajectory. When these electron-ion pairs are subjected to the influence of the electric field in the chamber, the electrons drift toward the nearest anode wires and the positive ions toward the field wires and the cathode plane.

Fig. 2.1 and Fig. 2.2 (generated by the simulation software GARFIELD[9]) show the electric field distribution inside a typical MWPC chamber geometry. The electric

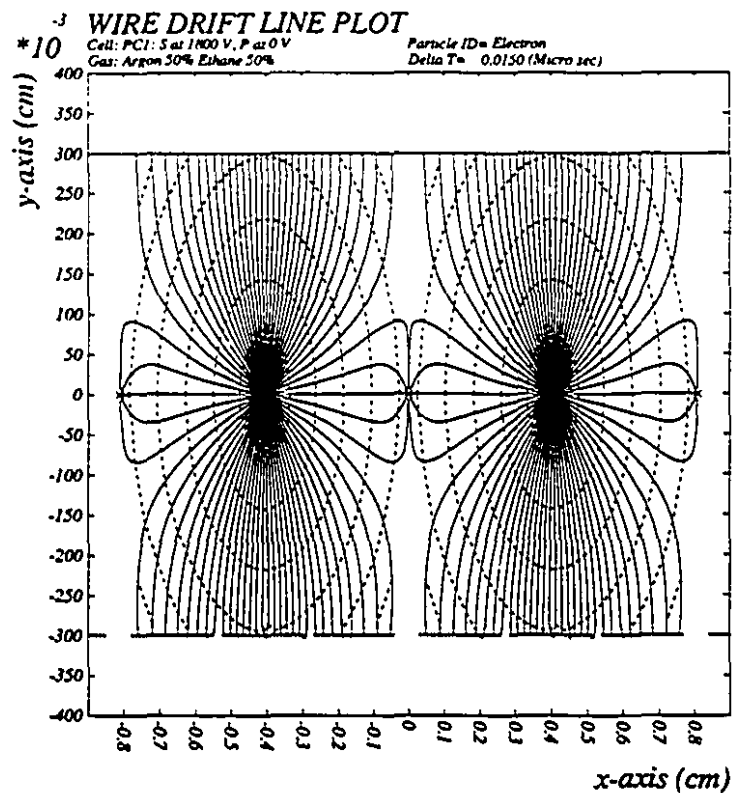


Figure 2.1: Electric field lines (solid line) and equi-time lines (dashed line) in PC1.

field inside the chamber is not uniform. With the increase of the electric field near the anode wires, the electrons gain more energy between collisions as they drift toward the anode wires. Eventually, when they collect enough energy which is greater than the ionization potential of the gas molecules, they can ionize the gas molecules upon collisions and consequently create additional electron-ion pairs. If these processes continue on, an avalanche of ionization will eventually be formed. As illustrated in

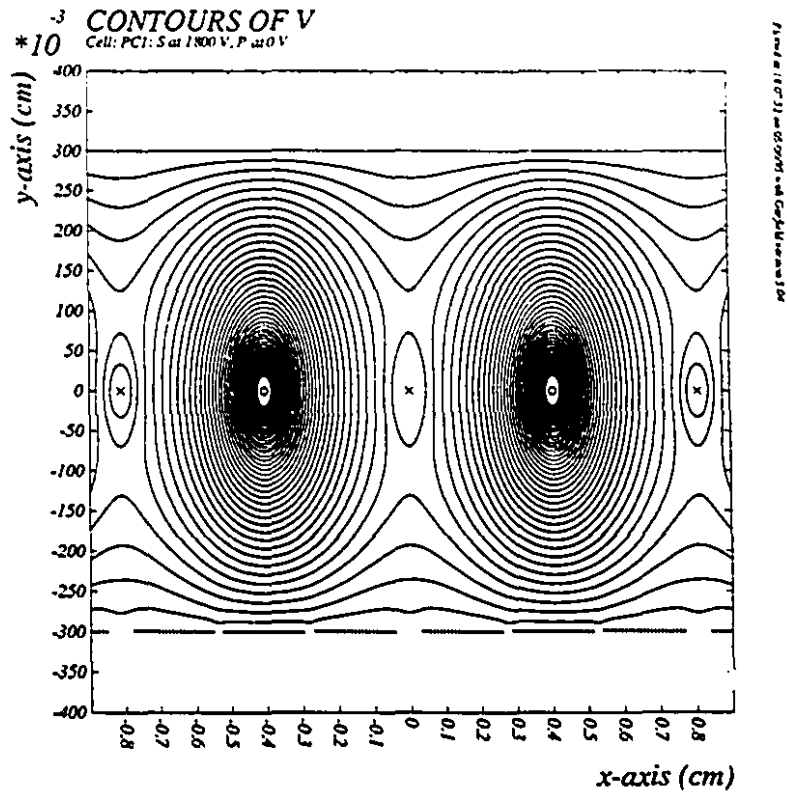


Figure 2.2: Equi-potential lines in PC1.

Fig. 2.2, the typical chamber has a cylindrical electric field near the anode wires. The avalanche normally takes place within several diameters above the anode wire surface.

At the same time, the created positive ions drift away from the anode wires. Comparing with the speed of the drifting of electrons, they can be considered stationary. If the avalanches create a large number of electron-ion pairs, the "stationary" posi-

tive ions can form a “shell”, which effectively reduces the electric field strength. This is called the space charge effect. This effect can reduce gas amplification.

2.3 Induced Charge on Electrodes

The movement of the electrons and positive ions from an avalanche induces charge on the surrounding electrodes. The detector readout electronics is normally connected to either the anode or one of the two cathodes.

A simple chamber geometry is shown in Fig. 2.3.

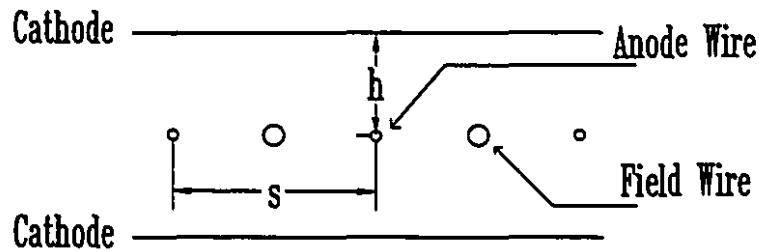


Figure 2.3: Pad Chamber Geometry Illustration.

Since most of the avalanche charges are created in the last few mean free paths of the primary electrons as they drift toward the anode wires, it is thus instinctive to consider the situation near the anode wire. Assume the radii of the anode and field wires to be r_a and r_c , respectively. With this simple situation, the electric field and

the potential inside the chamber, close to the anode wires, can be described as:

$$E(r) = \frac{1}{\ln(r_c/r_a)} \frac{V_a}{r} \quad (2.3)$$

$$V(r) = V_a \left[1 - \frac{\ln(r/r_a)}{\ln(r_c/r_a)} \right] \quad (2.4)$$

In which, we assume V_a is the anode wire voltage and V_c is the cathode voltage, which normally is at 0. Therefore, the signal current in the anode readout electronics is[10]:

$$\begin{aligned} i_a &= -q_0 \frac{1}{2 \ln(r_c/r_a) t_0} \times \frac{1}{1 + t/t_0} \quad (2.5) \\ t &\leq t_0 \left[\left(\frac{r_c}{r_a} \right)^2 - 1 \right] \\ t_0 &= \frac{r_a}{2\mu E_a} \\ E_a &= \frac{V_a}{r_a \ln(r_c/r_a)} \end{aligned}$$

in which, q_0 is the induced ion charge, μ is the positive mobility, defined in $v(r) = \mu E(r)$, where $v(r)$ is the velocity of the positive ion. If we extrapolate the cylindrical geometry to the cathode, for a two-electrode system, the signal current i_c in the cathode readout is:

$$i_c = -i_a = q_0 \frac{1}{2 \ln(r_c/r_a) t_0} \times \frac{1}{1 + t/t_0} \quad (2.6)$$

For systems with multiple electrodes, the induced charge is distributed among many electrodes. For a plane cathode geometry as illustrated in Fig. 2.3, the induced charge density distribution on the cathode plane, can be calculated with the simple

image charge method[11]. With the parameters described in Fig. 2.3, it can be written as:

$$\rho(x, y) = -\frac{Q_A}{2\pi} \sum_{n=0}^{+\infty} (-1)^n \frac{(2n+1)h}{[(2n+1)^2 h^2 + x^2 + y^2]^{\frac{3}{2}}} \quad (2.7)$$

where Q_A is the total negative avalanche charge. The charge distribution along any one dimension can be therefore derived by integrating Eq. 2.7 over the other dimension.

2.4 Pad Chamber With Geometrical Charge Division

Conventional MWPC with a single anode wire plane “sandwiched” by two plane cathodes gives positional information of the incident particles in the dimension perpendicular to the wires, and the position resolution is governed by the anode wire pitch, which can be shown to be $\sigma = s/\sqrt{12}$ [12], where s is the anode wire spacing in the wire plane. In the interpolating method, the charges imaged on the cathode are shaped according to the geometrical shape and pattern of the cathodes, and this pattern or structure can give position information much better than the traditional one. Interpolating methods can be divided into three categories: resistive charge division, capacitive charge division and geometrical charge division. Among those, geometrical charge division has the most reliable high resolution and linearity in a high multiplicity of charged tracks environment.

MWPC with geometrical charge division uses electrodes with specially shaped geometrical pattern to sample the avalanche charge. The amount of charge induced on the electrodes shaped between different segments of the pattern varies with the position of the avalanche. Therefore, very good position resolution can be achieved. Fig. 2.4 shows some of the many variations of those special shaped electrodes providing the readout signals.

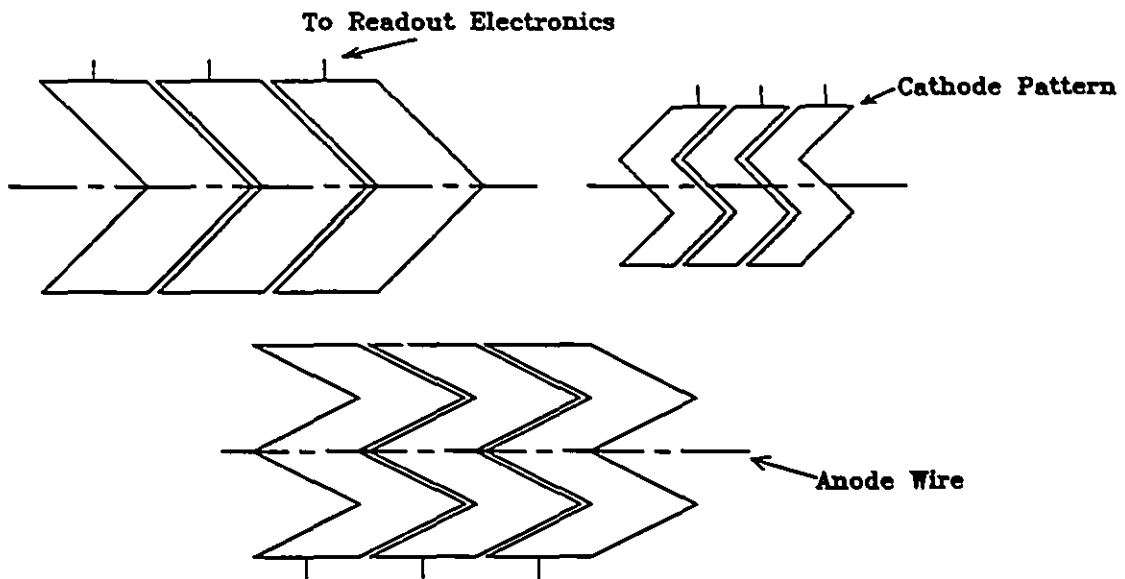


Figure 2.4: Examples of the Chevron Pad Pattern.

Chamber with these kinds of cathode readout is called chevron cathode chamber. During the first phase of this pad chamber work, an extensive research and development work were carried out on this kind of chevron pad chambers at McGill University[13]. This work has led to the successful construction of a large size pro-

prototype chamber. According to this research, PHENIX pad chamber with chevron cathode option can offer good position resolution in the order of 1%-1.5% of the readout spacing, the same for the position linearity[14]. However, the construction for the chevron pad chamber requires high accuracy etching of the cathode board with chevron pad geometry. The high cost per readout channel to keep the requirement of high precision analog readout electronics is offset by the relatively few channels due to large chevron pad size to cover a given spatial area. However, the large pad size also makes them less ideal for double track resolution, i.e., separating two tracks. If the chevron size is decreased to improve the two-track resolution capability, the number of channel to cover the same area would increase dramatically, so would the cost. However, this decrease in pad size and increase in channel count would be acceptable if a way could be found to decrease the readout electronics cost per channel. On the basis of present electronic technology, this would necessitate the use of electronic system other than the high precision analog electronics. This is achievable by using a digital readout system with highly integrated CMOS chips. To minimize the cost for a system with large number of channels, these CMOS chips could be used in the "unpackaged" or "based" chip form and mounted directly on the readout cathode board. This is called the chip-on-board, COB, technology. Using this technology, a factor of ten reduction on cost per channel could be achieved, comparing with the cost of the high precision analog readout system. For example, in a typical analog readout system, the cost per channel is about \$40, whereas the digital readout system

using COB technique cost about \$4 per channel. In a typical pad chamber system in the PHENIX detector using chevron shaped pad cathode, the channel count is about 50,000, giving rise to a total cost of about \$2,000,000. For the same cost, one can have a pad chamber system with digital readout system of 500,000 channels.

If one could have a pad chamber system with sufficiently large enough number of pads, there would then be no need to make the pads chevron shaped. One can simply make the pads rectangular shaped with dimension along and perpendicular to the anode wire comparable to the spatial resolution desired. However, this would require about one million pads or channels for the pad chamber system for PHENIX. To make the system more manageable and affordable, a scheme was derived to split each rectangular pad into three smaller rectangular pads, called pixels, and three pixels under each anode wire is linked up like a stair case to form subpad. These subpads across three different anode wires are then electrically connected together to form a pad. The pads, staggered and interspersed with each other, form the whole cathode board. In this way, it is possible to design a pad chamber system for the PHENIX detector with a total channel number of about 240,000. The basic pad chamber scheme and the R&D work on it will be presented in the following chapters.

Chapter 3

The New Pixel Pad Chamber

The pixel pad cathode readout is a brand new readout scheme for the MWPC. The cathode plane is divided into many rectangular pixels and every nine of which are linked together to form a staggered pad from which the signal is obtained. With careful selection of the readout signals from these pads, the desired position resolution can be achieved. A special method adopted to link the pixels into pads also reduces the number of readout channels.

3.1 Principles of Operation of Pixel Pad Chamber

The basic structure of a pixel pad chamber is similar to the ordinary MWPC, with anode and field wires interspersed each other. Fig. 3.1 gives an overview of the chamber structure.

Fig. 3.2 illustrates the basic pixel pad cathode pattern. Every three adjacent

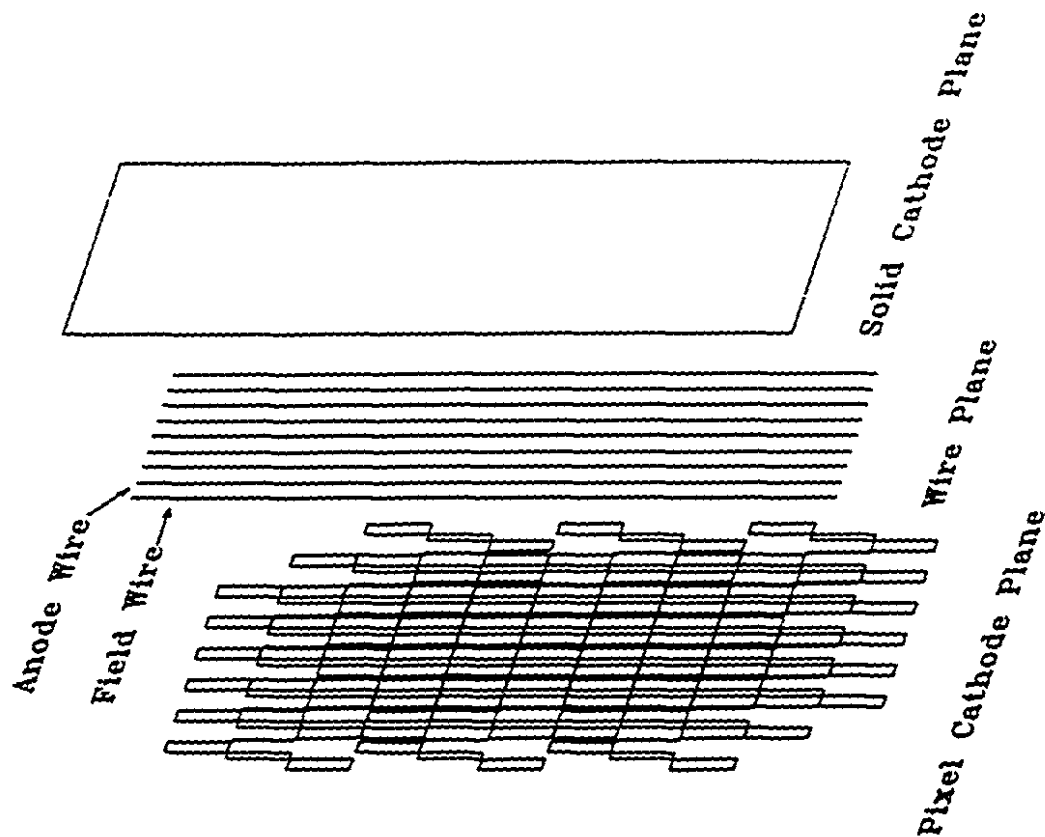


Figure 3.1: Overview of the Pixel Pad Chamber Structure.

pixels under one anode wire make up one cell. These pixels belong to three different staggered pads, each pad straddles three anode wires. Each cell counts of one center pixel and two symmetric side pixels. The widths of the center pixel and the two side pixels are chosen so as to keep the charge induced by the avalanche on the three pixels to be equal. The lengths of these pixels are identical and are chosen to meet the desired position resolution along the wires direction, while the wire spacing meets the spatial resolution in the $r - \phi$ direction.

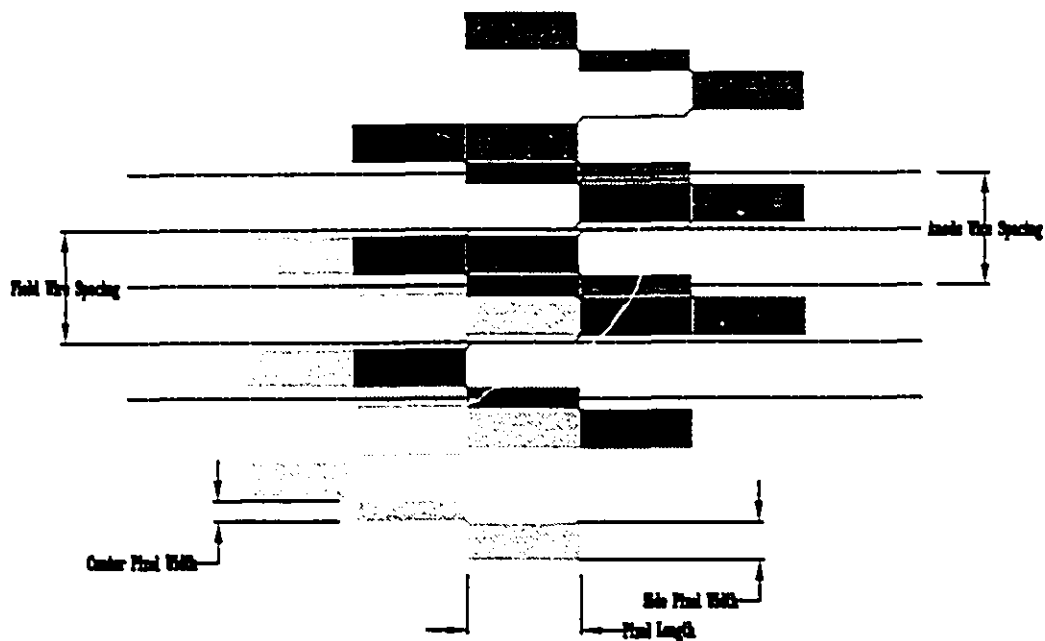


Figure 3.2: Pixel Pad Geometry Pattern.

For every single avalanche, the induced charge signals on both side pixels should be identical for symmetry reasons. Therefore, for each charge track inducing an avalanche will at least induce charges on all three pads associated with one cell and it is then said the cell is "fired". From Fig. 3.2, it can be seen that the situation with more than one cell fired at the same time is possible if the induced charge from a charged track overlaps more than one adjacent cell. When examining the signals from the pads, a cell is considered fired only if all three pads associated with it are fired at the same time. Since only the identical digitized signal 0, not all three pads are fired, or 1, all three pads are fired, is produced, no further measurements for the induced charges within one cell are taken. If one single cell is detected fired, one

reconstructed position for the track is assigned in the center of the fired cell. Because the adjacent cells belonging to two different anode wires are separated by a field wire which in principle should prevent "crosstalk" between anode wires, except for those tracks which traverse the border between two cells, ideally there shouldn't be more than two cells along an anode wire fired at the same time. When an avalanche induced by a charged track occurs at a location where signals are observed on four adjacent pads, two adjacent cells should be found fired. Therefore, the hit should be identified in the middle of the two cells. Since the image charge of an avalanche is more or less a Gaussian distribution on the pixel cathode, the exact number of pads fired for a given track is dependent on the avalanche charge size and the detection level setting of the readout electronics. It is entirely possible to have several cells fired for a single track in reality. However, in principle, the position resolution should be better than one-half cell size.

The readout electronics system is divided into two parts: the front-end electronics (FEE) part and the data acquisition (DAQ) part. The FEE is to process the signal from each channel by converting it into a digital bit, feeding it into a pipeline while a logic decision is being made on the validity of the signal and then deciding how and when to give the signal hit to the next stage. The DAQ is to accept the good signal bit from the FEE and process the data bit in a practical format for data analysis. The FEE for one channel is illustrated in Fig. 3.3.

The signal is fed to a 16-channel charge sensitive preamplifier and shaper, whose

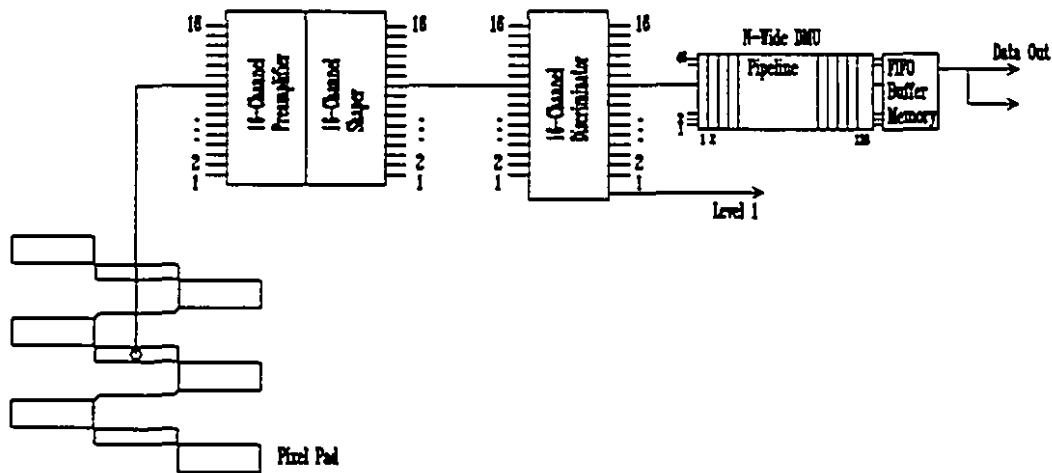


Figure 3.3: Front-End Electronic Readout for Pixel Pad Chamber.

output is connected to a 16-channel discriminator, where a bit in bit pattern is set. The bit pattern is then fed into a memory pipeline and clocked at a predetermined frequency, called the beam clock through a digital memory unit, DMU, followed by a FIFO buffer unit. When the signal bit reaches the end of the pipeline, a decision on the validity of the signal must be made. Following that, the data acquisition process is conducted to transfer all the digital data to computer.

3.2 Measures of Detector Performance

3.2.1 Position Identification

As mentioned before, in principle, at least one cell is always fired for every avalanche. The reconstructed position is determined by the distribution of the fired cells. How-

ever, the situation with more than one cell fired has to be considered, especially for cases in which the avalanche charge signal is large, a situation often encountered in this in-beam tests. A fired cluster is identified if one or more adjacent cells are found fired. For every distinguished cluster, one reconstructed position is determined according to its geometric shape. By setting the limit for the cluster size to a square of 3×3 cells, the following 24 different kind of clusters and their corresponding assigned reconstructed positions are specified as displayed in Fig. 3.4:

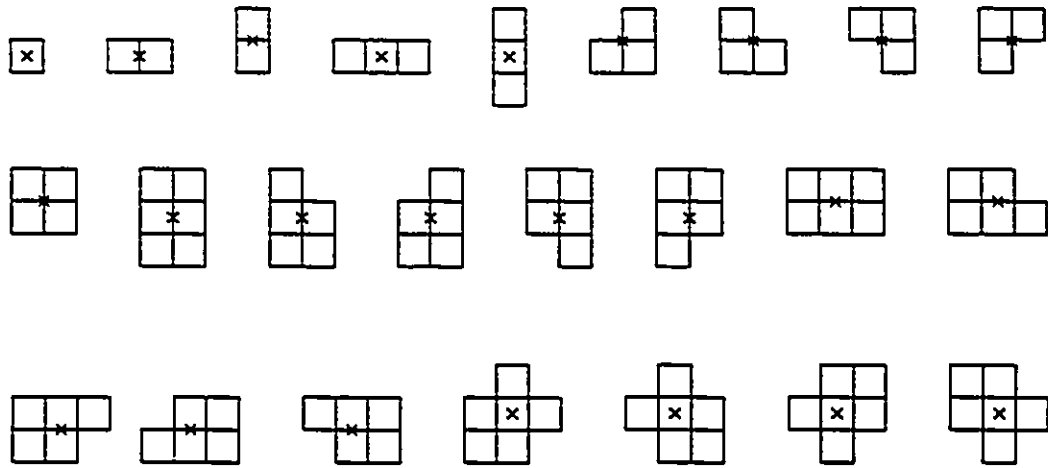


Figure 3.4: Cluster Classification.

3.2.2 Position Resolution

The ability of the detector to reproduce the positions of the charged tracks is called position resolution. It is defined as the standard deviation σ or the full width at half maximum ($FWHM = 2.36\sigma$) of the reconstructed position distribution for a

given incident particle whose position distribution is a δ - function. In real data, the position resolution is taken as the standard deviation σ or the full width at FWHM of the distribution of the deviation of the reconstructed positions from the true positions, where the distribution is taken to be a standard Gaussian distribution. In principle, for uniform incident particles, the position resolution of a conventional MWPC is given by the anode wire pitch, $\sigma = s/\sqrt{12}$ [12]. For the pixel pad chamber, in principle the position resolution along the wire is better than one-half of the pixel size.

3.2.3 Position Linearity

Assume the reconstructed position y of a track is a function of the true position x , $y = f(x)$. Then, with a normalized uniform irradiation source, the normalized uniform irradiation response (UIR), $v(y)$ is given by[15]:

$$v(y) = \frac{1}{f'(x)} \quad (3.1)$$

in which $f'(x)$ is the derivative of the function $f(x)$, the slope of the curve of $f(x)$. For an ideal linear position sensing detector, $f'(x) = 1$, so $v(y) = 1$. For the real detector, the differential non-linearity (DFNL) is used to measure the non-linearity.

$$DFNL = \frac{v_{max} - v_{min}}{(v_{max} + v_{min})/2} \quad (3.2)$$

Where v_{max} and v_{min} correspond to the maximum and the minimum values of UIR spectrum corresponding to the minimum and maximum values, respectively, of the slope of the true versus reconstructed position curve. DFNL is a quantity which can be measured and used to compare the deviation of a detector from the ideal linear response detector. A large DFNL could be caused simply by a "kink" in the response function over a small distance, which implies the large "non-linearities" of the chamber.

Chapter 4

Detector Construction

Two prototype pixel pad chambers, PC1 and PC3, were built in McGill University. The pixel pads of both detectors were designed to have geometric sizes as close to as their final version of the full scale pad chambers, to be used for the PHENIX experiment. They differ from their final ones only in the overall chamber sizes. Prototype PC1 has approximately one-quarter the size of the final unit sector detector, while prototype PC3 is approximately equal to one eighth of its final unit sector detector.

4.1 Design and Fabrication of Pixel Pad Chamber

4.1.1 Pixel Pad Chamber Design Consideration

	PC1	PC3
Pixel Length (mm)	8.2	16.45
Side Pixel Width (mm)	2.7	5.5
Center Pixel Width (mm)	1.5	3.0
Adjacent Pixel Spacing (mm)	0.25	0.25
Cell Spacing between Pixel Columns (mm)	1.0	2.0
Pixel Corner Cut (mm)	0.2	0.2
Pixel Interconnection Line Width (mm)	0.2	0.2
Plated-through Hole Diameter (mm)	0.3	0.3

Table 4.1: Pixel Pad Parameters

In an ideal situation where there is no limitation on the channel count and cost, the detector always performs better with a finer granularity, i.e., with a maximum number of pixel pads. The maximum number is determined by requiring each pad contains only one pixel and the pixel dimensions are consistent with the spatial resolution, both along the anode wire and perpendicular to the anode wire, of the detector. In this case, the rectangular pixels are lined up in a column beneath each anode wire, and the pixel columns are separated by space lines above which are field wires located in

the same plane as the anode wires. A pad chamber system for the PHENIX detector made this way would require a million pads or channels if the spatial resolution in both directions for PC1, PC2 and PC3 equaled to $\pm 4mm$, $\pm 7mm$, and $\pm 5mm$, respectively, were met. In an effort to reduce the channel number and cost, each squared pixel is split into three rectangular pixels across the wire direction, and the pixels beneath each anode wire are joined together like a 3-step stair case. One stair case from each of three adjacent anode wires, are then connected together to form a 9-pixel pad as illustrated in Fig.3.2. The pads are staggered in such a way that the position of the charged track that traverses each cell is distinct. This connection scheme has allowed the reduction of channel count for the PHENIX pad chamber system by a factor of three.

To test the workability of the scheme and the performance of such a detector, two prototype pixel pad chambers of approximate dimension $20cm \times 90cm$ were designed and fabricated: one resembled the geometry of PC1 and the other of PC3. The dimension of the three pixels in each cell under an anode wire were chosen to give the two side pixels the same width and the center pixel a narrower width so that three pixels would receive equal image charge from a centrally located avalanche around the anode wire. The pixel pad sizes for PC1 and PC3 are summarized in Table. 4.1. The chambers dimension parameters are summarized in Table. 4.2.

	PC1	PC3
Anode Wire Diameter (μm)	25	25
Field Wire Diameter (μm)	125	125
Anode-to-Anode Wire Spacing (mm)	8.4	16.5
Anode-to-Field Wire Spacing (mm)	4.2	8.25
Anode Wire to Cathode Spacing (mm)	3.0	6.0
Active Cathode Plane Width (mm)	188.3	167.5
Active Cathode Plane Length (mm)	781.65	739.05
Guard Ring Width (mm)	1.0	1.0
No. of Anode Wires	22	10
No. of Field Wires	23	11
No. of Readout Cards	16	4
No. of Readout Channels	768	192

Table 4.2: Pixel Pad Chamber Parameters

4.1.2 The Pixel Cathode Board Design

The pixel cathode board was made of a $250\mu\text{m}$ thick FR4 fiberglass sheet with printed circuit on both sides. The copper thickness on each side was $8.6\mu\text{m}$. The two sides were connected with plated-through holes for channel readout. A basic pixel cathode unit for the prototype PC3 is given in Fig. 4.1.

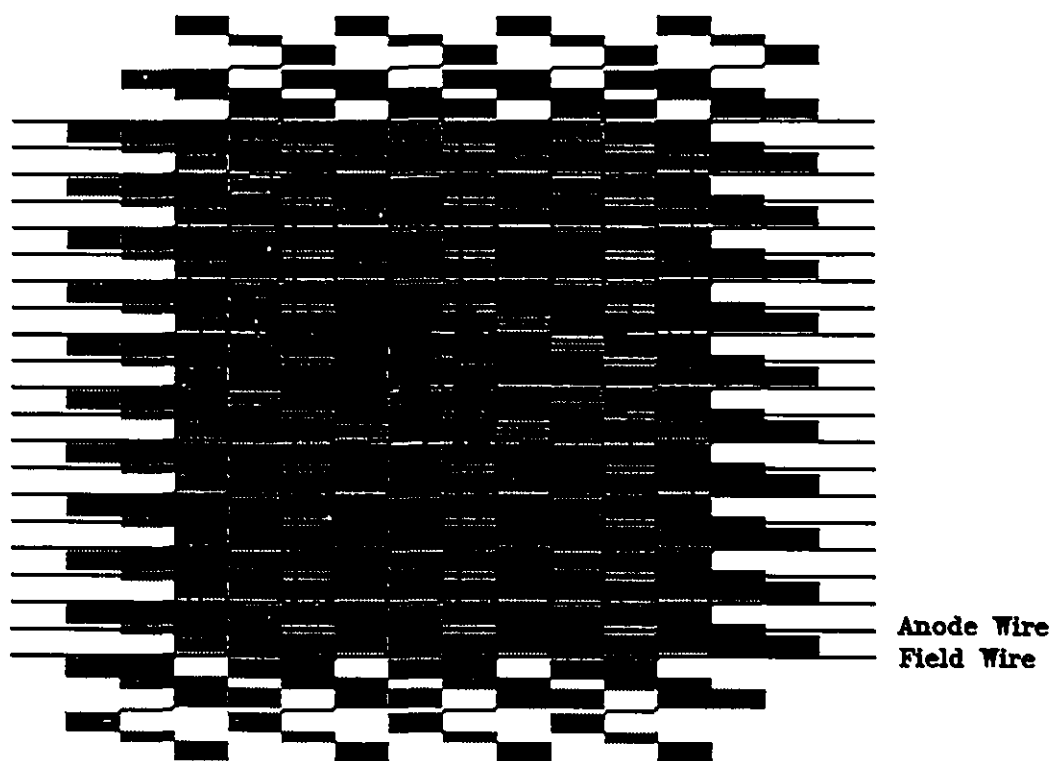


Figure 4.1: The Basic Readout Unit.

The bottom side of the board was the pixel cathode side and the top side was its corresponding signal connection side shown by the black lines. It could be seen that this basic structure had a 10-cell \times 10-cell arrangement, or 48 channels. Therefore, it was convenient to use this structure as one readout unit and the card that contained all this readout FEE was called a readout card. If the pixel size and wire spacing were chosen properly, the entire cathode board would be fabricated by duplicating this basic structure throughout the board. When the basic structure was at the edge of the board, these pixel pads which staggered outside the center square of 10-anode-wire \times 10-pixel were cut approximately, and the 48 readout channels per unit remained the same. Those incomplete pads less than 9 pixels at the edges were connected specially according to their original connection patterns. Traces from the plated-through holes on the back of the pixel board (top side) were led to the surface-mounting micro-connectors. For every 48-channel readout unit, there were four surface-mounting connectors: two right-angle ones soldered on the top side of the pixel cathode board, and the other two vertical ones soldered on the motherboard, which contained all the FEE readout electronics, attached to the back of the pixel cathode board. All connectors had 26 pins with spacing of 0.5 mm. This basic pixel cathode unit was same for the prototype PC1 too, except for the connection pattern on the top.

The numbering sequence of the FEE readout channels was in the numerical order of the connector pins, as presented in Fig. 4.2. This FEE channel numbers had a

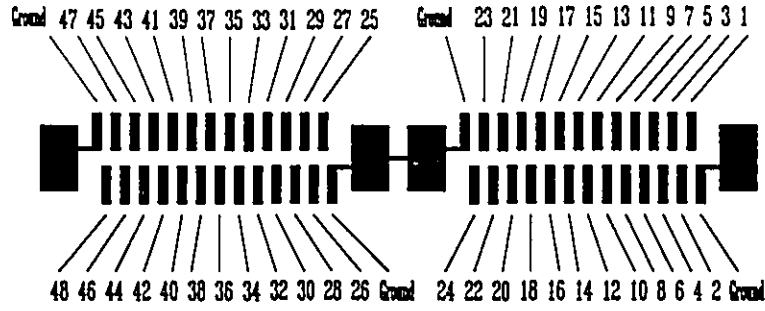


Figure 4.2: FEE Readout Channel Numbering on Connector Pins, viewed from the top side of the pixel cathode board.

different mapping onto the topological location of the pixel pads for PC1 and PC3, simply because of the space problem to accommodate the readout cards. This FEE channel to pixel pad location mappings for PC1 and PC3 are shown in Fig. 4.3. They are also different from their final detectors, although the final detectors PC1, PC2 and PC3 do have the same readout scheme.

The pixel cathode boards for the prototype PC1 and PC3 are shown in Fig. 4.4 and Fig. 4.5 respectively. One can see both the top and bottom sides of the boards.

4.1.3 The Motherboard Design

The motherboards for prototypes were also made of $250\mu\text{m}$ FR4 fiberglass double sided printed circuit boards, with the bottom side just a ground plane and the top side contained all the electronic circuit traces. The copper thickness on each side was $8.6\mu\text{m}$. The FEE were housed on the readout card which were mounted on the

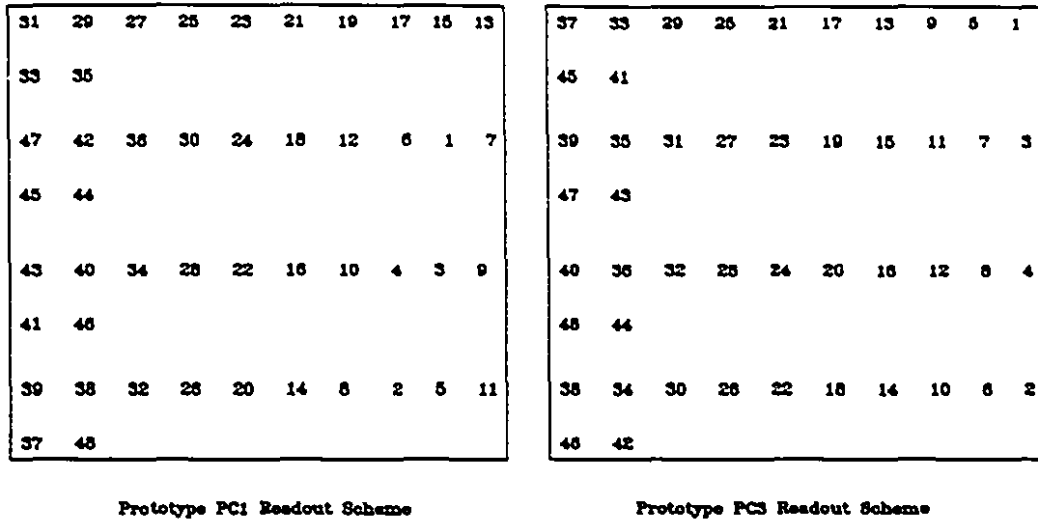


Figure 4.3: FEE Readout Channel Numbering on Pads, viewed from the top side of the pixel cathode board.

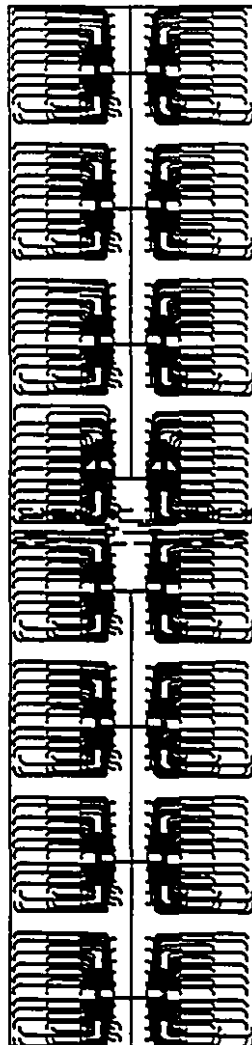
motherboard. For each readout card, there was an opening hole on the motherboard for the high-pitch kepton cables carrying the signals from the back of the pixel board to the connectors on the motherboard. The hole had a dimension of $1.0\text{cm} \times 3.5\text{cm}$. The kepton cable were specially designed, each contains 26 traces of 0.5mm pitch. In order to simulate the data readout arrangement of the final detectors, the data of the prototype chambers were also read out through both ends of the motherboard and then fed to the DAQ system. The printed circuit board design for the PC1 motherboard and PC3 motherboard are shown in Fig. 4.6 and Fig. 4.7.

Board type: FR4
 Board thickness: 0.010"
 Copper weight: 1/4 oz
 Dimensions are in mm
 All Holes: 0.4 mm in diameter
 Double side board.



Bottom View

Mirror Line

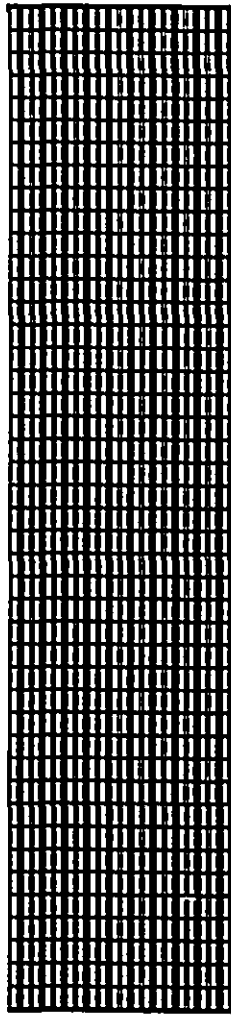


Top View

PIXEL1.DWG August 1995

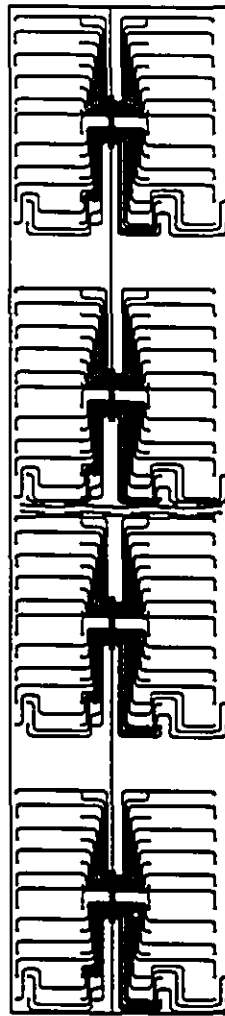
Figure 4.4: PC1 Pixel Cathode Board Design.

Board type: FR4
 Board thickness 0.010"
 Copper weight 1/4 oz
 All dimensions are in mm
 Double side board
 All Holes are 0.4 mm in diameter



Bottom View

Mirror Line



Top View

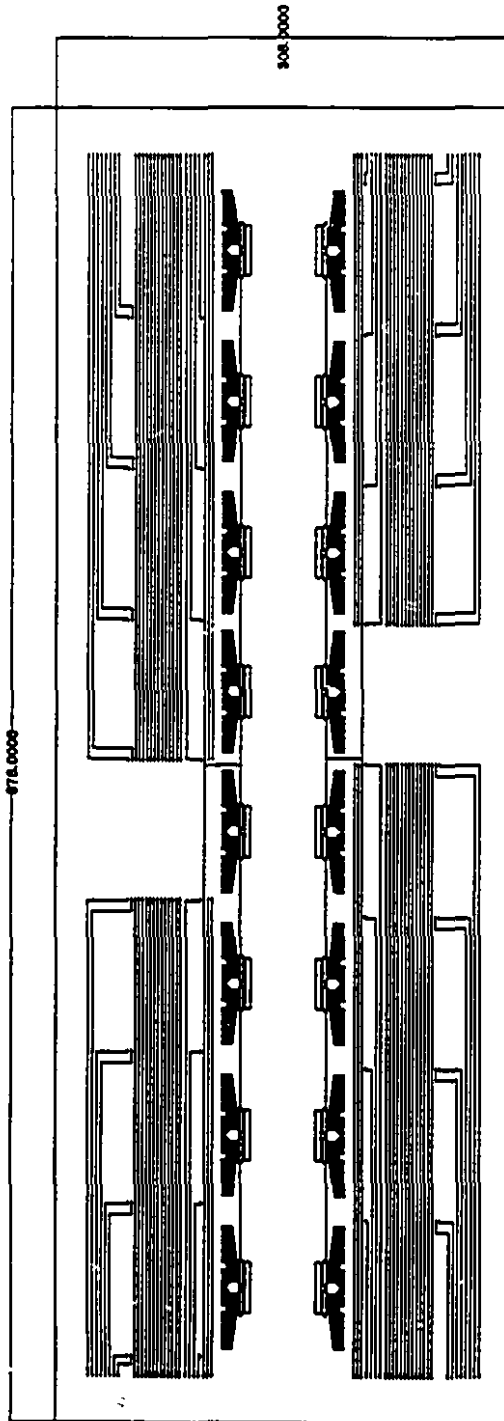
PIXEL.DWG August 1986

Figure 4.5: PC3 Pixel Cathode Board Design.

Board thickness: 0.010"
 Copper weight: 1/4 oz
 Dimensions are in mm
 Double side board.
 Bottom side is pure copper (no traces).

Top View

47A.0000



308.0000

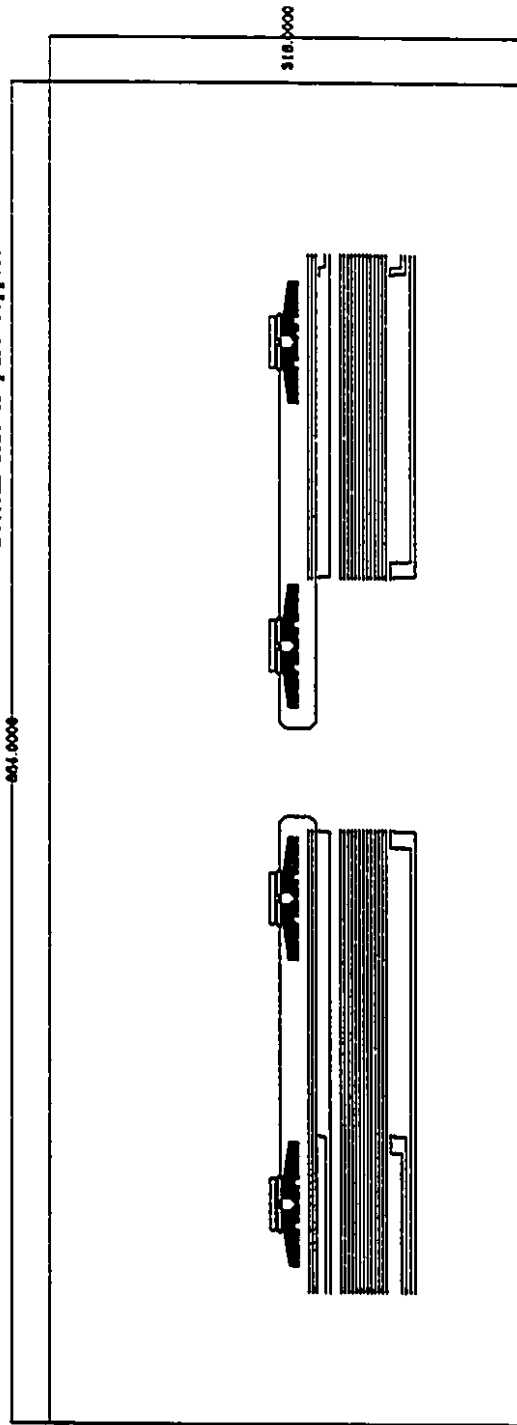
MOTHER1.DWG August 1995

Figure 4.6: PC1 Motherboard Design.

Board type.....FR4
 Board thickness.....0.020"
 Copper weight.....1/4 oz
 All dimensions are inmm
 Double side board.
 Bottom side is pure copper.

Top View

804.0000



MOTHER3.DWG August 1995

Figure 4.7: PC3 Motherboard Design.

4.1.4 Chamber Assembly

The mechanical structure of prototype PC1 and PC3 chambers were similar. The illustration for the cross section of the chamber is given in Fig. 4.8.

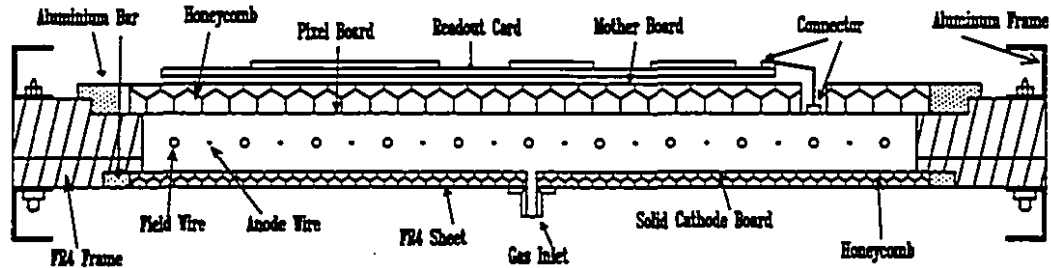


Figure 4.8: Cross Sectional View of the Mechanical Structure of the Prototype.

The fabrication procedures for these prototype chambers were also similar. While these small prototypes were built manually, however, for the fabrication of the large final detectors, large machines would be required to assist in the production.

The fabrication process for the chambers took place in a “clean room” with class 10000 air filters. The major fabrication steps in the manufacturing of the prototypes were summarized as following¹:

1. After careful examination of the connection of all the plated-through holes on the pixel cathode board made of $250\mu\text{m}$ FR4 fiberglass, they were covered with conducting glue to prevent gas leakage.
2. Surface-mounting micro-connectors were soldered on the pixel cathode board

¹Not necessarily follow this order.

and the motherboard.

3. A piece of one inch thick honeycomb with prepared cutouts for the passage of the multi-conductor, high pitch kepton cables and four anodized aluminum supporting frames were glued together on the back side of the pixel cathode board. This procedure was performed on a high precision flat granite table.
4. The motherboard was glued on top of that honeycomb.
5. The high-pitch kepton cables were plugged into the surface mounted connectors on both the pixel cathode board and the motherboard.
6. The electrical connection between the channels on the pixel cathode board and those on the motherboard was thoroughly examined with multimeter.
7. After this pixel cathode panel was completed , it was mounted on the FR4 fiberglass frame shown in Fig. 4.9 and Fig. 4.10.
8. At the same time, two pieces of printed circuit boards, each of $250\mu m$ thick fiberglass, one piece with $8.6\mu m$ thick copper on one side, and a piece of quarter inch thick honeycomb, were glued together to make a "sandwich" panel, which was called the solid cathode panel.
9. After the gas connectors were laid on the solid cathode panel, they were mounted on another FR4 frame shown in Fig. 4.11.

10. Two high-precision pitch bars were glued on the top of the pixel cathode board to guide the wires, which were precisely aligned with respect to the pixel columns.
11. Wires passing through these pitch bars were soldered on the terminal boards glued at each end on top of the pixel cathode board.
12. The whole assembly was ascertained of dust free before the two FR4 frames were closed.
13. Finally, the FEE readout cards were soldered on top of the motherboard.
14. High voltage was then applied to the anode wires with gas flowing the chamber to test static performance.

Up to here, the chambers were successfully assembled.

4.2 Detector Electronics

Specially designed data readout cards, each contained 48 channel of front-end electronics, were housed on the detector mother board to data out these chambers. The data were read out from both ends of the motherboard and fed into a data acquisition system. All the readout cards were read in parallel and each card gave its data output in serial.

4.2.1 Readout Card

Each readout card contained 48 channels of FEE electronics, which comprised of three 16-channel preamplifier/shaper chips, TGL, three 16-channel discriminator chips, DISCR, and one 48-channel digital pipeline memory unit, DMU, chip, equipped with five fold buffer, FIFO. All the chips were high pitch ($2\mu m$ per channel) CMOS chips. The TGL chips were charge sensitive preamplifier and shaper that converted charge signals from the pixel pads to voltage signals and shaped them into pulses with a decay time constant of about $500ns$. The DISCR chips were simple level discriminator which produced pulses of standard height but varying width depending on the length of time the input signal pulse exceeding the threshold voltage level. Both the TGL+DISCR chips were designed and fabricated at the Oak Ridge National Laboratory (ORNL).

The DMU/FIFO chips were 48-channel CMOS chips manufactured at Lund University, Sweden. In the DMU part, each pipeline memory channel was programmable up to 128 cells deep and the buffer, FIFO, was a 48-channel 5-event memory. The DMU pipeline was clocked through its memory cells by a clock running at a predetermined frequency that was adjustable up to $20MHz$. But in this work, the clock was set at $2MHz$. When a digital signal appeared at the output of a DISCR channel and latched into the corresponding DMU channel, it triggered an external decision logic. When the DMU driven by the clock reached its last memory cell, a decision logic signal called LVL1 coming from the external logic circuit must appear at the output

circuit of the DMU in order for the original charge digital signal from the DISCR to be passed onto the buffer memory. The buffer event memory of each DMU/FIFO chip was then read out serially by an read-enable logic signal to the data acquisition system. The logic structure was illustrated in Fig. 4.12.

4.2.2 Timing Logic

The timing sequence of the operation of DMU in the real in-beam tests was drawn in Fig. 4.13. When the particle came at beam_clock 0 as shown, the charge signals were converted and shaped to voltage signals by the TGL and then converted to the standard height pulses by the discriminator, DISCR, all just in a few beam_clocks. Then, they were stored in the 128 cells deep delay memory. At beam_clock 128, the LVL_1 went to high, at the next beam_clock, the "oldest" three bits of pulses were pumped into the event memory at beam_clock rate. Then at beam_clock 132, the readout decision was made, the out_enable went to low, and at the same time, the read_clock was started. The read_clock was set to be one third of the frequency of the beam_clock. After a few moments delay, the serial outputs were started to be read out. For every event, 64 bits were read out to accommodate the possible changes of the readout scheme of the 48 channels for each card, with another additional one error-checking bit, total of 65 bits were read out. When all the 65 bits were finished, at beam_clock 327, the out_enable went to high again, and the DMU_Reset went to low to reset the DMU to be ready for the next event. At this time, the whole process

for one event readout was finished within 327 beam_clocks.



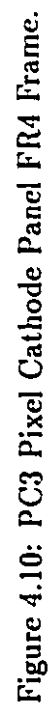


Figure 4.11: PC1&PC3 Solid Cathode Panel FR4 Frame.

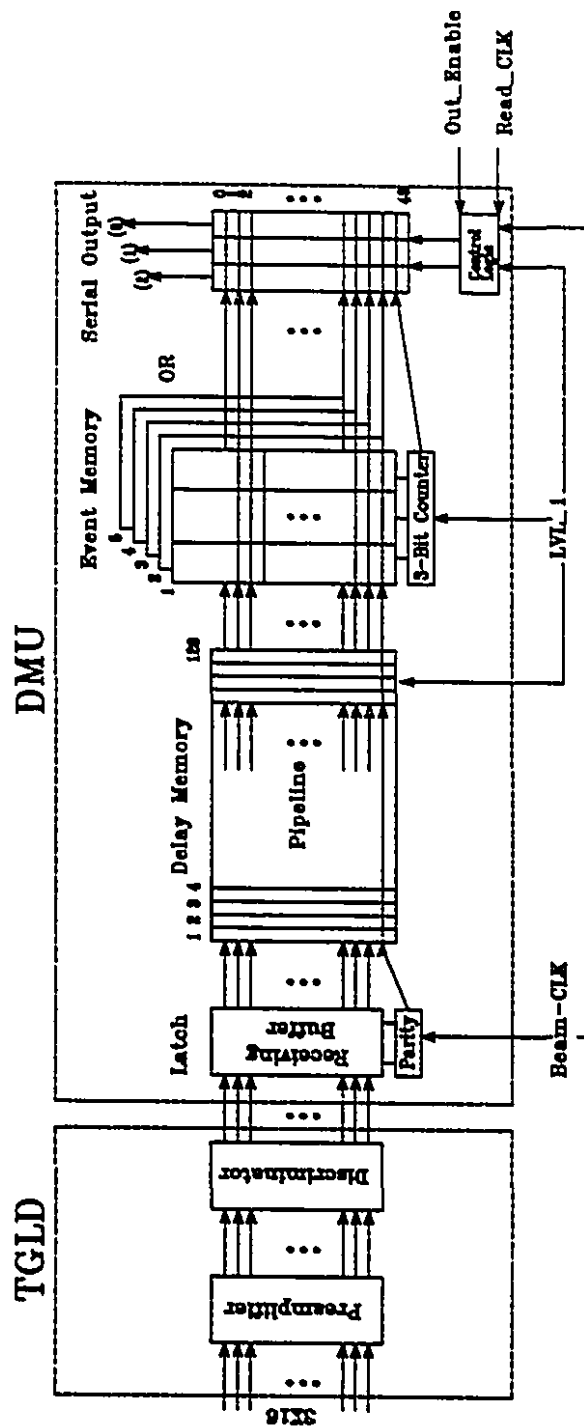


Figure 4.12: FEE of Readout Card Logic Structure.

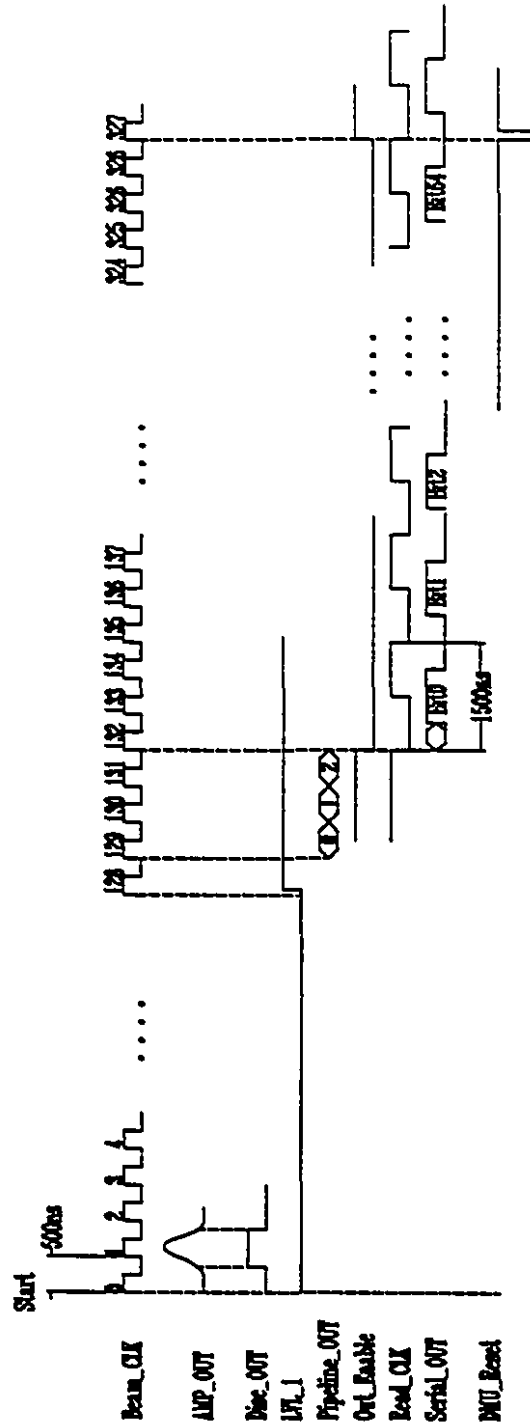


Figure 4.13: DMU Function Description in Timing Sequence.

Chapter 5

In-beam Tests

The prototypes were first tested on the bench-top using a X-ray source and then tested in B2 beam line of the Alternating Gradient Synchrotron (AGS) at BNL using a secondary beams of electrons, (e^-), muons, (μ^-), and pions, (π^-) of various momenta between 0.5 and 10*GeV/c*. It lasted for 15 days, from March 8th to 23rd, 1996. The data presented here were analyzed during the months of April and May, 1996.

5.1 Experiment Setup

The B2 beam line at the AGS is a facility dedicated to secondary beams induced by the 32 GeV proton beam. Secondary beams of e^- , μ^- and π^- were available over wide range of momentum up to 10*GeV/c*. There were three beam defying scintillation counters (S1, S2, S3) and a high resolution tracking chamber in the beamline

(Fig. 5.1). S1 and S2 had an effective area of $5\text{cm} \times 5\text{cm}$, and S3 of $10\text{cm} \times 10\text{cm}$. The tracking chamber was a two-dimensional gas proportional detector[16] with a resolution less than $300\ \mu\text{m}$. It was used to give the true particle position in the x-y plane perpendicular to the beams. During the normal measurements, the beam intensity was always controlled to give a coincidence count rate of about 100/sec.

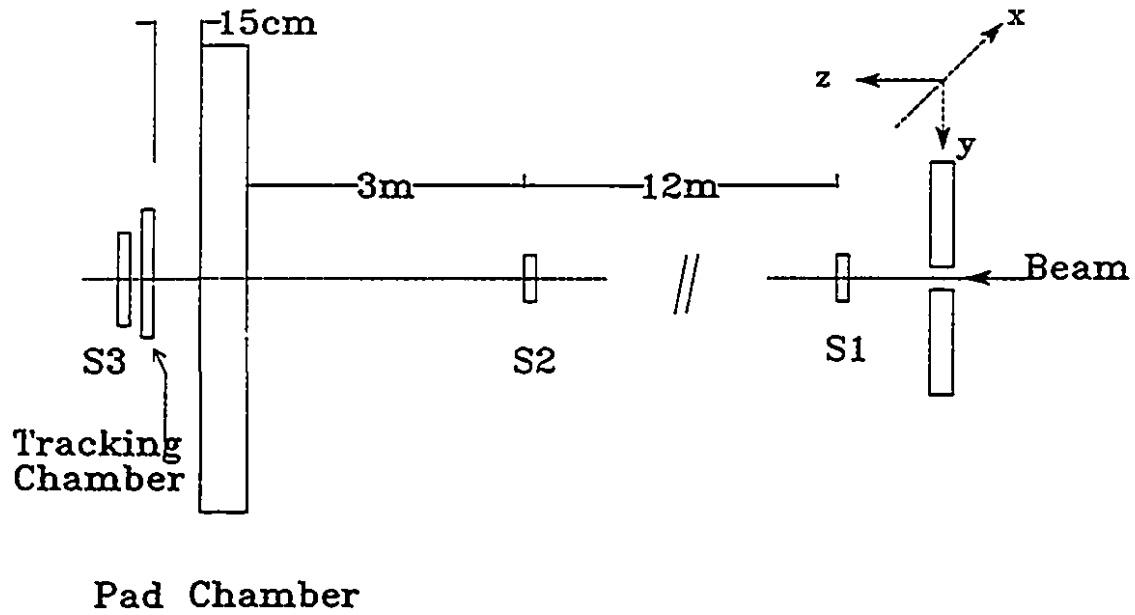


Figure 5.1: Beam Line Setup (See text for details).

The gas used in the test was 50% Argon and 50% Ethane. The detectors were mounted on a moving platform operated by a servomechanism to provide a two dimensional motion in the x-y plane. Both PC1 and PC3 chambers were scanned along the wires, which were oriented in the x direction. The PC1 detector mounted in the beamline viewed upstream against the beam is shown in Fig. 5.2. The 16 FEE

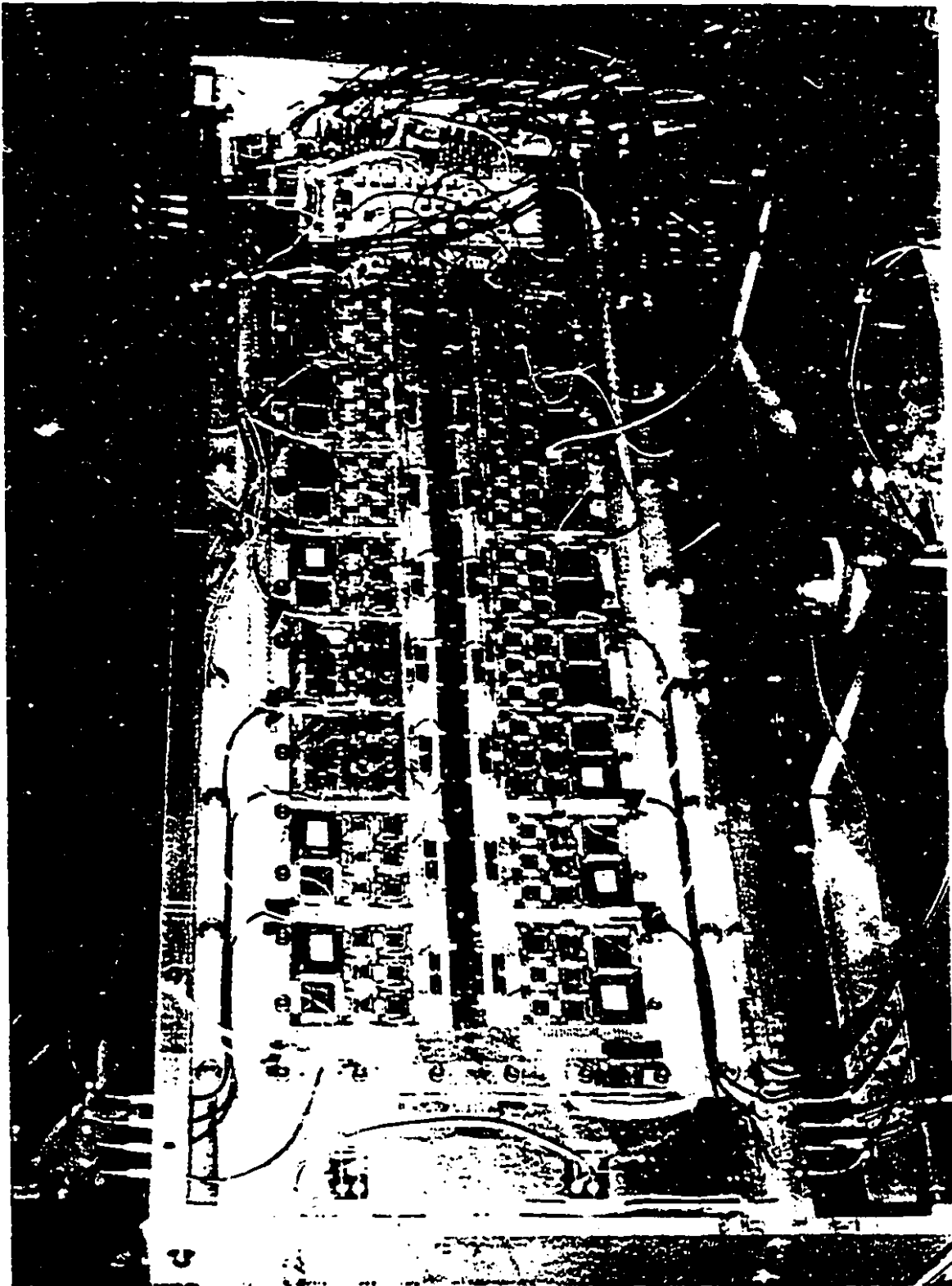


Figure 5.2: Photograph of PCI in Beamline.

readout cards for every 16 channels were mounted as shown on the motherboard. The DAQ systems were controlled by an IBM PC-486 connected to the VME crate. The logical DAQ systems are drawn as Fig. 5.3.

5.2 Detector Characteristics

The pixel pad chamber is a new kind of MWPC. Much of the chamber characteristics was unknown before. Several ways were tried to study the performance of these two chambers. Noise study was carried with a particular run for PC3 with external pulse triggers without beam. Study of the type of pad clusters induced by charged particles can give clear view about the hits pattern in the beam test. Comparing the reconstructed positions with the positions provided by the precision tracking chamber can give information about the position resolution and linearity of the chambers. Overall effective reconstructed position is a good measurement of the chamber efficiency. The high voltage and threshold effects on the response of the chamber was also studied.

5.2.1 Noise Study

A typical run for PC3 was recorded without beams to study the noise effect for our chamber. The coincidence triggers were generated by a pulser. The results are given in Table. 5.1.

The high voltage at this test was 2200V and discriminator threshold was set to 1.15V, which was equivalent to real voltage threshold of 33mV, which was supposed

Total No. of Events	47000	
No. of Events with Fired Pads	8477	18.0%
No. of Events with Fired Cells	991	2.1%

Table 5.1: Noise Study for PC3.

to be the same for all chips in all the readout cards. This 2.1% fired cells included all the background noise at that particular location. It is not surprising at the beam line area. Because of the noise level in both PC1 and PC3 was relatively high, due mostly to pick-up and switching coupling, it was not possible to set the threshold voltage of the discriminators at value less than 1.15V or real threshold 33mV.

5.2.2 Cluster Characteristics

To test the response of the chambers to the beam of e^- , μ^- and π^- particles, a beam giving about 100 counts per second was allowed to fall on the chambers under test. Fig. 5.4 and Fig. 5.5 are typical hits pattern distributions of the pads and cells for PC1 and PC3, respectively. The numbers shown on the axis are the numbering orders of the pads and the cells in the two dimension chambers. For the pads, the nine connected pixels (one channel) were numbered only once. The bigger the box in the diagram, the larger number of events a particle hit the particular pad or cell.

The statistical pattern of detected pads, cells and clusters fired by the beams are presented in Fig. 5.6 and Fig. 5.7. From those diagrams, it can be concluded that

large number of pads, cells, as well as clusters were fired in approximately the same as expected. A surprisingly large number of fired pads did not make up effective cells.


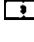






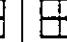


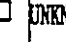
The large number of events with fired cells and that of no fired cells showed strong dependence on the thresholds setting of the discriminator chips. From Table. 5.2, it can be seen that, even at the lowest permissible real threshold $V_{th} = 33mV$, the chambers still missed 28.4% events for PC3 and 72.6% events for PC1. In general, the detection efficiency increases as the threshold voltage decreases. The significant percentage of the events with zero fired cell in PC1 was traced mainly to the relatively low signal strengths. The PC1 could only operate at 1750V high voltage during the beam tests because of the contamination of the chamber. No efficient avalanche was formed at this voltage for many of the low amplitude signals. Besides this, for both PC1 and PC3, there were several other factors such as the presence of dead channels, large variation in discriminator triggering level among different channels and timing misadjustment in the DAQ systems which could have also contributed to the total missing events.

Of all the clusters of cells detected, the distribution of cell patterns were identified and classified, and the results are listed in Table. 5.3. According to this table, although the events with single cell fired were still the most frequent, it was much less than expected. For both chambers PC1 and PC3, cluster patterns with the multiple cells fired with cells across the wires occurred more often than those patterns with cells along the wires. In the case of double-cell clusters, their comparison was

	V_{th}	$No_{FiredCell} = 0$	$0 < No_{FiredCell} < 9$	$No_{FiredCell} \geq 9$
PC1	33 mV (1.15 V)	72.6%	24.7%	2.7%
PC3	26 mV (1.20 V)	21.3%	43.2%	35.5%
PC3	33 mV (1.15 V)	28.4%	56.3%	15.3%
PC3	45 mV (1.00 V)	50.6%	43.2%	6.2%

Table 5.2: Fired Cells Category. $HV = 1750V$ for PC1, $HV = 2200V$ for PC3 .

17.6% to 6.7% for PC3, and for triple-cell clusters, this comparison became 12.1% to 1.1% at the normal high voltage of 2200V and discriminator threshold of 33mV. A close explanation of Table. 5.3 revealed that, for both chambers PC1 and PC3, the double-cell clusters which straddled two anode wires and those which oriented along one anode wire were comparable. This is expected because the cell dimensions are more or less square and the probability for a charged track traverses the border of two adjacent cells should be comparable. Since the charged particle beams entered the detectors perpendicular to the plane of the detectors, normally a track can only fire one or two adjacent cells and nearly impossible to fire three adjacent cells, particularly for those straddle three adjacent anode wires. Most of the observed clusters containing three adjacent cells either straddled three anode wires or along an anode wire were probably induced by two charged tracks. If this was the case, one may deduce from Table. 5.3 that there were about 18% double-track events in the PC3 measurements.

	V_b													UNKNOWN
PC1	33mV (1.15v)	70.3%	11.0%	10.1%	1.4%	2.2%	1.0%	2.0%	0.4%	0.9%	0.4%	0.3%	0.02%	0
PC3	26mV (1.20v)	42.3%	14.0%	16.1%	3.9%	8.1%	3.4%	5.7%	1.6%	2.8%	0.4%	1.2%	0.4%	0.1%
PC3	33mV (1.15v)	52.8%	6.70%	17.6%	1.1%	12.1%	2.3%	1.8%	1.5%	3.3%	0.1%	0.4%	0.3%	0
PC3	45mV (1.00v)	53.0%	14.6%	13.2%	2.7%	4.8%	4.2%	2.5%	0.7%	2.4%	0.5%	1.0%	0.3%	0.1%

* With Four Variation

Table 5.3: Fired Clusters Classification.

5.2.3 Position Resolution

The primary purpose of the pad chamber is for the use to determine the two-dimensional position of the incident charged particles. To establish the reference positions, called true positions, for all the charged particles, a well calibrated tracking chamber (See Fig. 5.1) was used in conjunction with the pad chamber. The difference between the reconstructed positions from the pad chambers and the “true” positions from the tracking chamber were fit into a Gaussian distribution. The distribution thus obtained from the raw data without any correction is presented in Fig. 5.8 for PC1 and Fig. 5.9 for PC3. It is obvious that in the direction across (perpendicular to) the wires, some large errors existed, which distorted the Gaussian distribution. The large errors were probably due mostly to large clusters of fired cells induced by two closely spaced tracks. To eliminate events with multiple tracks, selection was made on events with an avalanche signal in only one anode wire or in two adjacent anode wires within beam area together with only those events giving good tracking

signals and with a single reconstructed cluster of fired cells less than 9. The results achieved are shown in Fig. 5.10 and Fig. 5.11. The efficiency of the tracking chamber itself was only 75%. The events with clusters made up of very large number of fired cells or events with multiple clusters were ignored because they mainly came from the shower of particles induced by the incident beams hitting some material along the beam path. Giving consideration to the possible variation in the chamber properties from one anode wire to another, the best results were achieved in the way that all the reconstruction procedures were carried out only under one anode wire. The best results achieved for a single wire are shown in Fig. 5.12 and Fig. 5.13, which is also summarized in Table. 5.4. The results obtained for both chambers along the wires direction are comparable with the half length of the pixel sizes.

PC1		PC3	
σ_x (cm)	σ_y (cm)	σ_x (cm)	σ_y (cm)
0.548	0.468	0.776	0.707

Table 5.4: Best Measured Position Resolution.

5.2.4 Position Linearity

The difference between the reconstructed position X_{rec} and the coordinate X_{true} given by the tracking chamber is given in Fig. 5.14 and Fig. 5.15 for PC1 and PC3 respectively, as a function of the avalanche location along the wires. Only half of the

size of PC1 chamber was scanned for this purpose. The one-dimension projection of the position errors gave the global position resolution $\sigma_x = 0.763cm$ for PC1 and $\sigma_x = 1.375cm$ for PC3. They were all in the direction along the wires.

The non-linearity showed a basic linear pattern around every chamber location. It can be partially explained by the scheme how the reconstructed position was assigned to every identified clusters. Since the reconstructed position was always given in the middle of the clusters, every time when the true position was larger than the reconstructed one, the difference gave a negative sign, when the true position was smaller than the reconstructed one the difference gave a positive sign, as simplified in Fig. 5.16.

5.2.5 Reconstruction Efficiency

The total reconstructed efficiency dependence on the total avalanche charge was also studied. As shown in Fig. 5.17 and Fig. 5.18, the efficiency of both chambers depended strongly on signal strength. Evidently, the chamber were not efficient at all at low signal size, i.e., the detection of low charge signals was flawed. Even at relatively large signals, the efficiency seemed to plateau at about 65% for PC1 and at 60% for PC3. The following factors could contribute to the low efficiency:

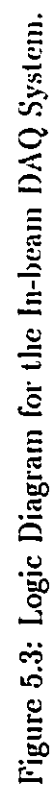
1. The low high voltage in PC1 induced small avalanche signals,
2. The dead readout channel effect, as each dead channel affected 9 cells in 3 different anode wires,

3. The crosstalk.
4. The large channel-to-channel variation in the triggering efficiency in the discriminators of the front-end electronics.
5. The DAQ inefficiency caused by the timing jitter and bad adjustment.

Because of the limited time in the beam test, much more detailed study about this inefficiency was missed. A more direct explanation of this low efficiency observed is expected after the current x-ray source tests of these two chambers are completed.

5.2.6 High Voltage and Threshold Effects

The high voltages and discriminator thresholds effects on the number of fired pads and cells were also investigated for PC3. They are shown in Fig. 5.19 and Fig. 5.20. At $HV = 2200V$, it was seen that the actual discriminator voltage threshold at 26 mV (1.20 V) gave the largest number of cells fired, although many of them were far away from the "true" particle positions. This implies that many cells were fired by noise. When the high voltage, HV, was varied and the discriminator threshold was kept at 33mV (1.15V), the efficiency increased with voltage. It seemed that the efficiency increased significantly at $HV = 2200V$, around 60% of the events had fired cells. This is another demonstration of the efficiency of this chamber depending on signal height.



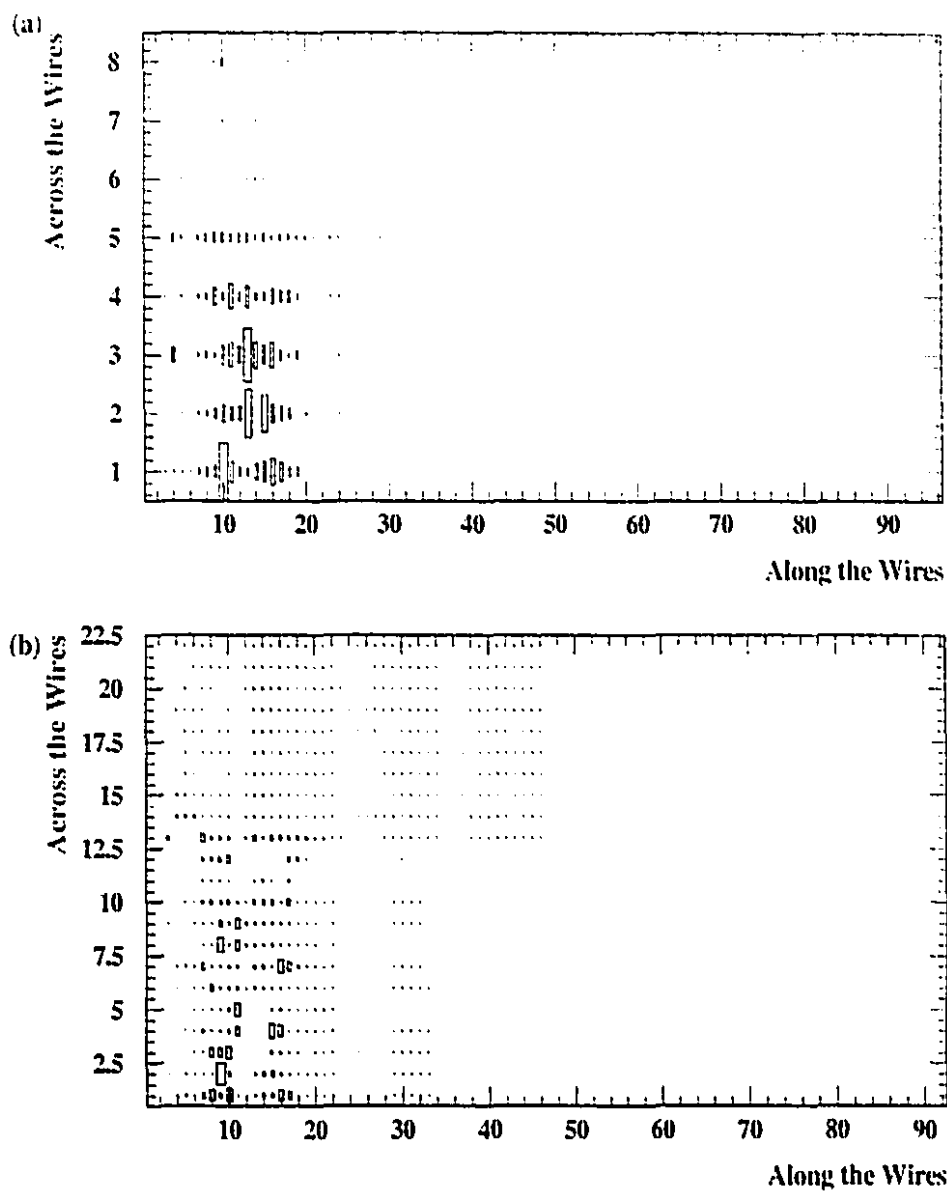


Figure 5.4: PC1 Hits Pattern. (a) PC1 Pads Hits Pattern; (b) PC1 Cells Hits Pattern.

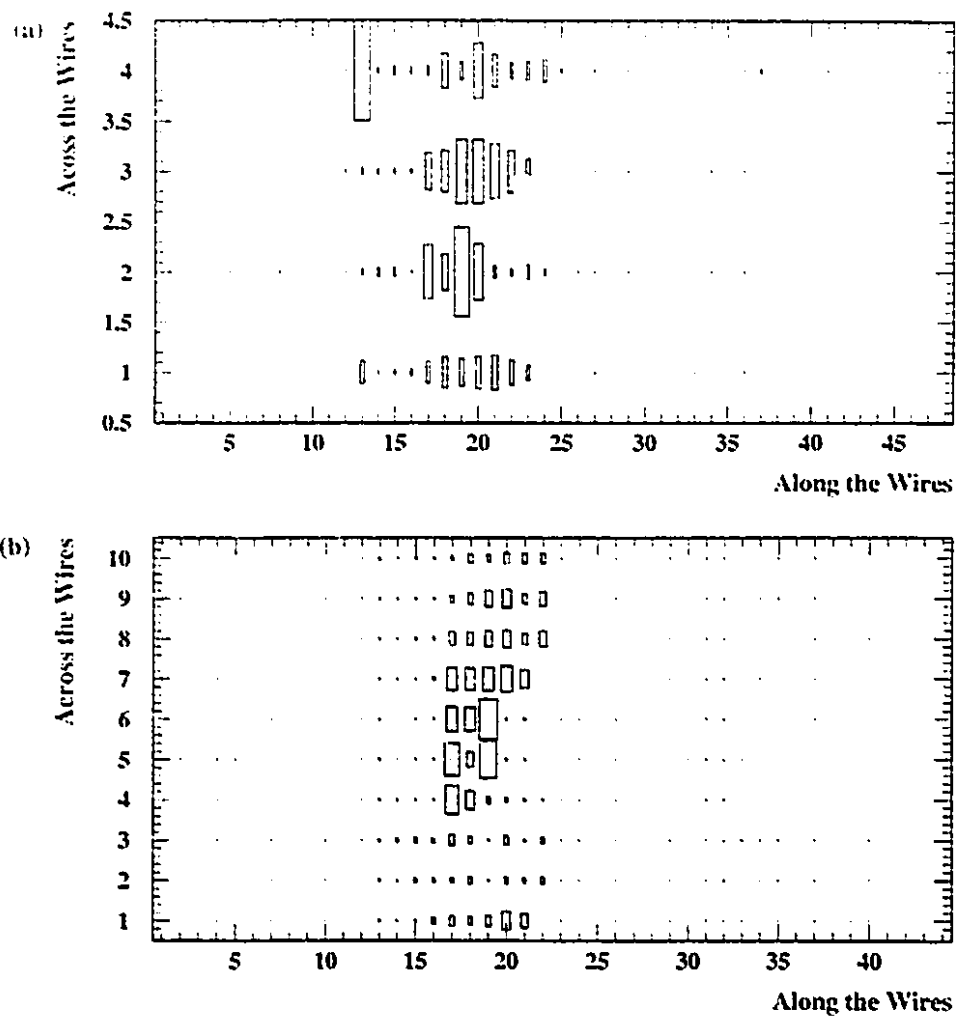


Figure 5.5: PC3 Hits Pattern. (a) PC3 Pads Hits Pattern; (b) PC3 Cells Hits Pattern.

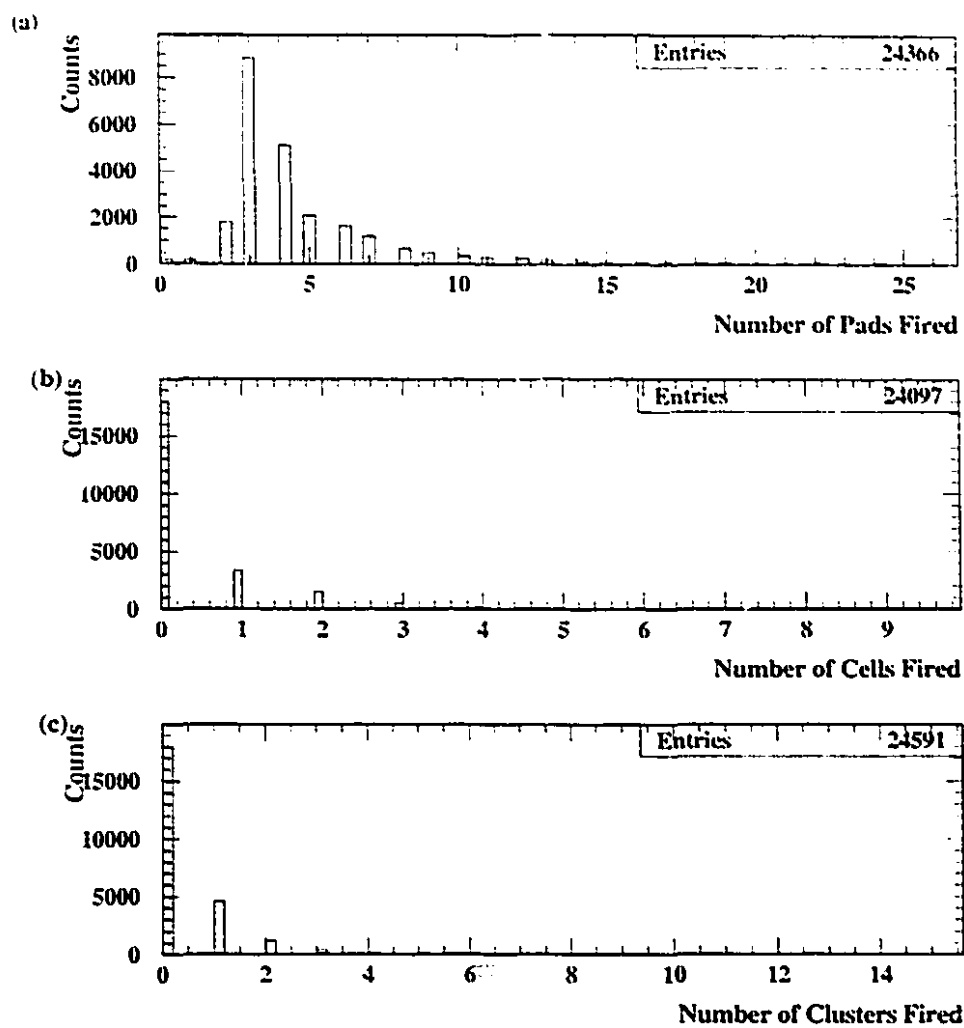


Figure 5.6: PC1 Hits Distribution. (a) PC1 Pads Fired; (b) PC1 Cells Fired; (c) PC1 Clusters Fired.

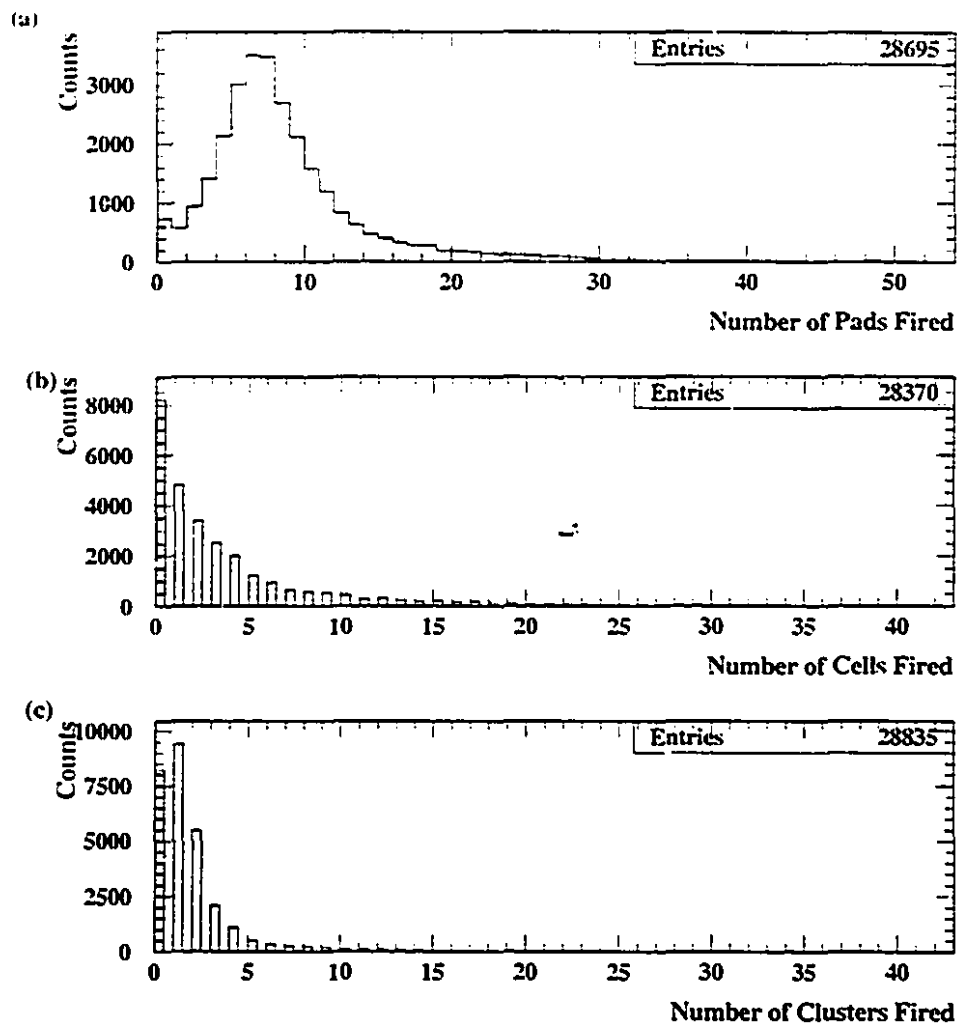


Figure 5.7: PC3 Hits Distribution. (a) PC3 Pads Fired; (b) PC3 Cells Fired; (c) PC3 Clusters Fired.

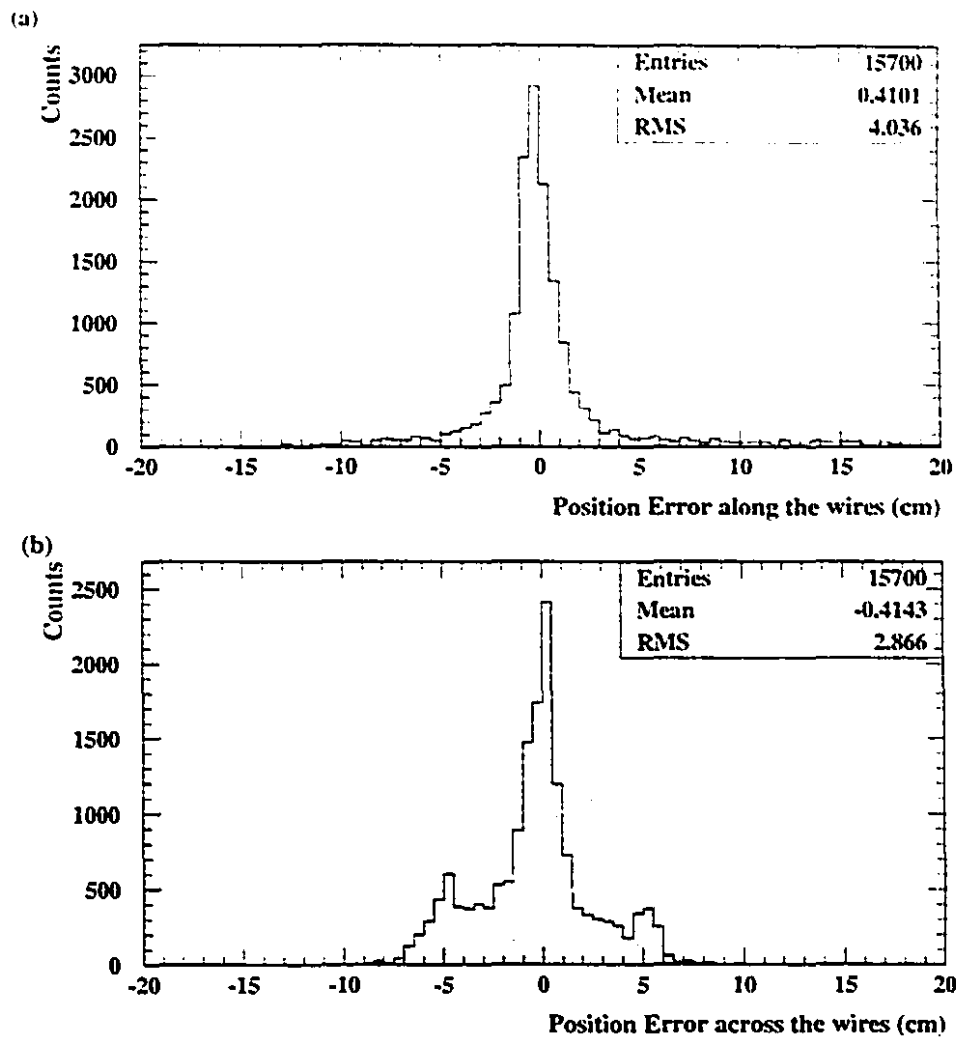


Figure 5.8: PC1 Raw Data for the Reconstructed Position. (a) Reconstructed Position Along the Wires; (b) Reconstructed Position Across the Wires.

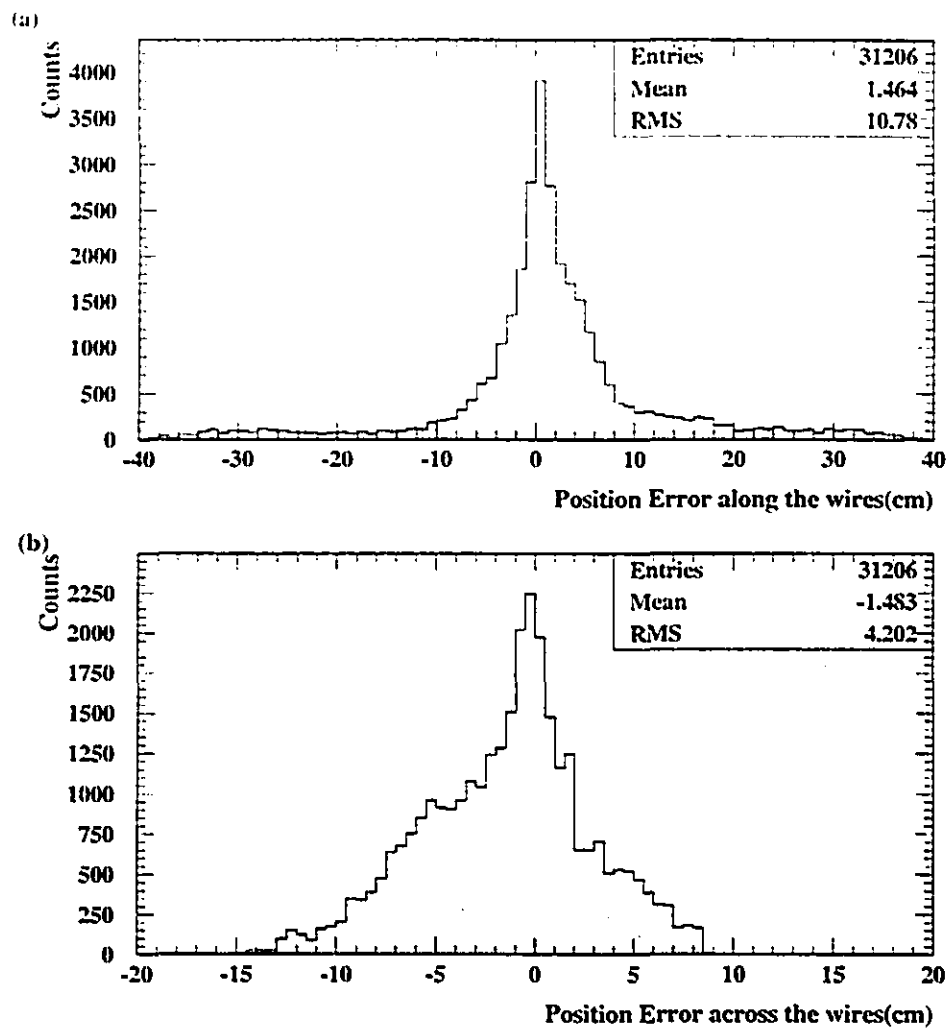


Figure 5.9: PC3 Raw Data for the Reconstructed Position. (a) Reconstructed Position Along the Wires; (b) Reconstructed Position Across the Wires.

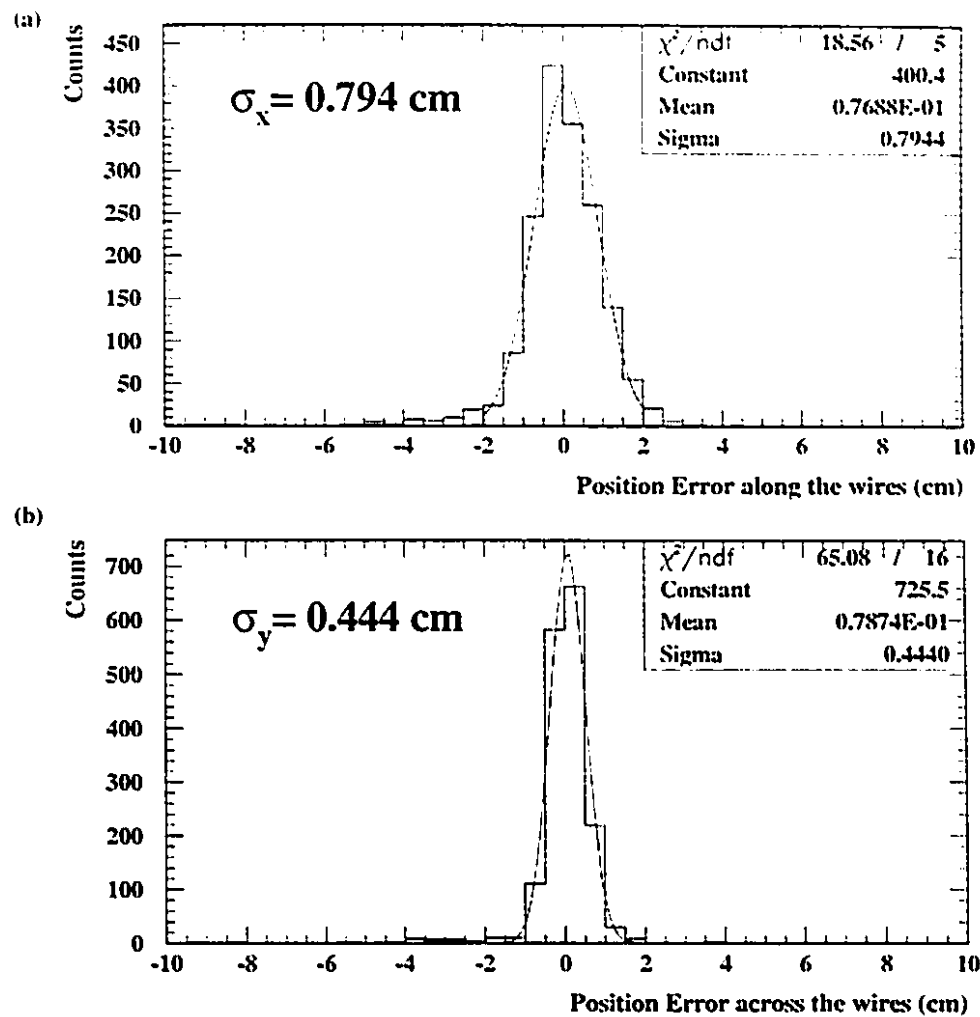


Figure 5.10: PC1 Reconstructed Position Resolution under Any Wire. (a) Reconstructed Position Resolution Along the Wires; (b) Reconstructed Position Resolution Across the Wires.

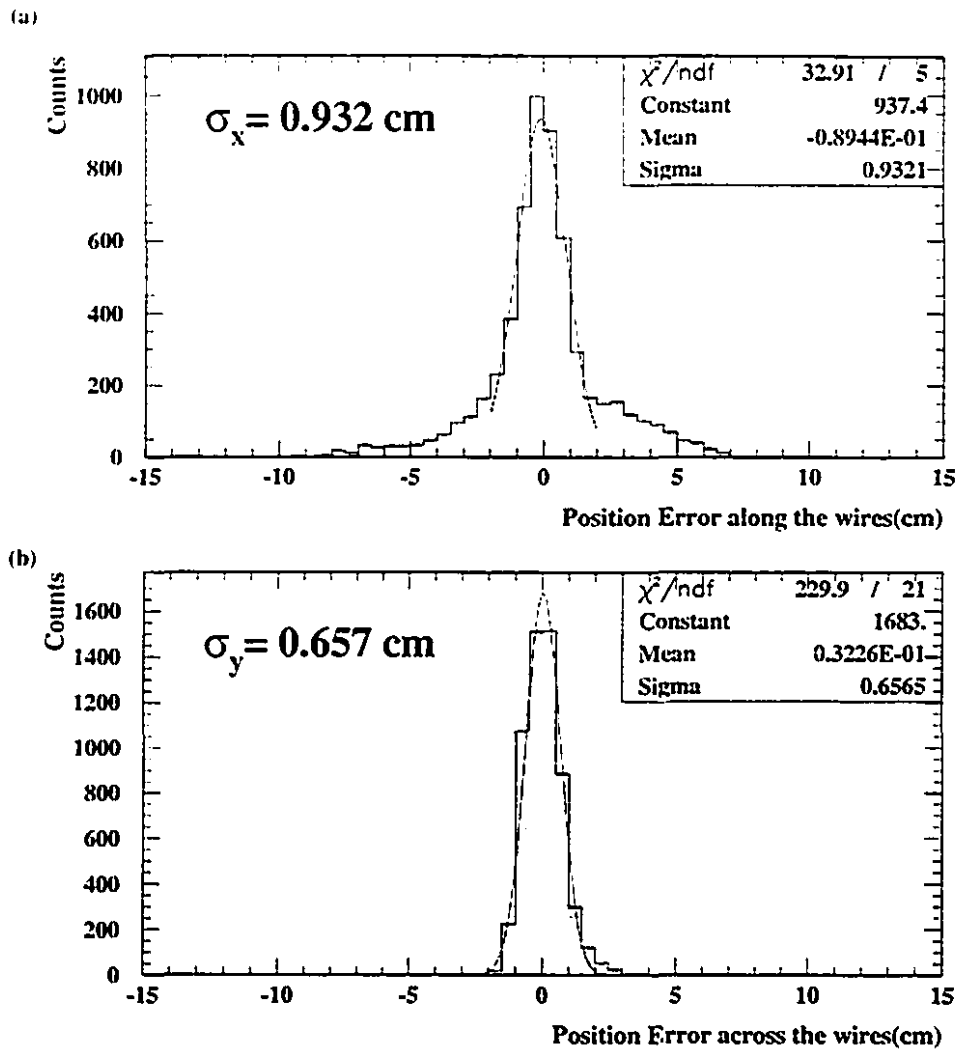


Figure 5.11: PC3 Reconstructed Position Resolution under Any Wire. (a) Reconstructed Position Resolution Along the Wires; (b) Reconstructed Position Resolution Across the Wires.

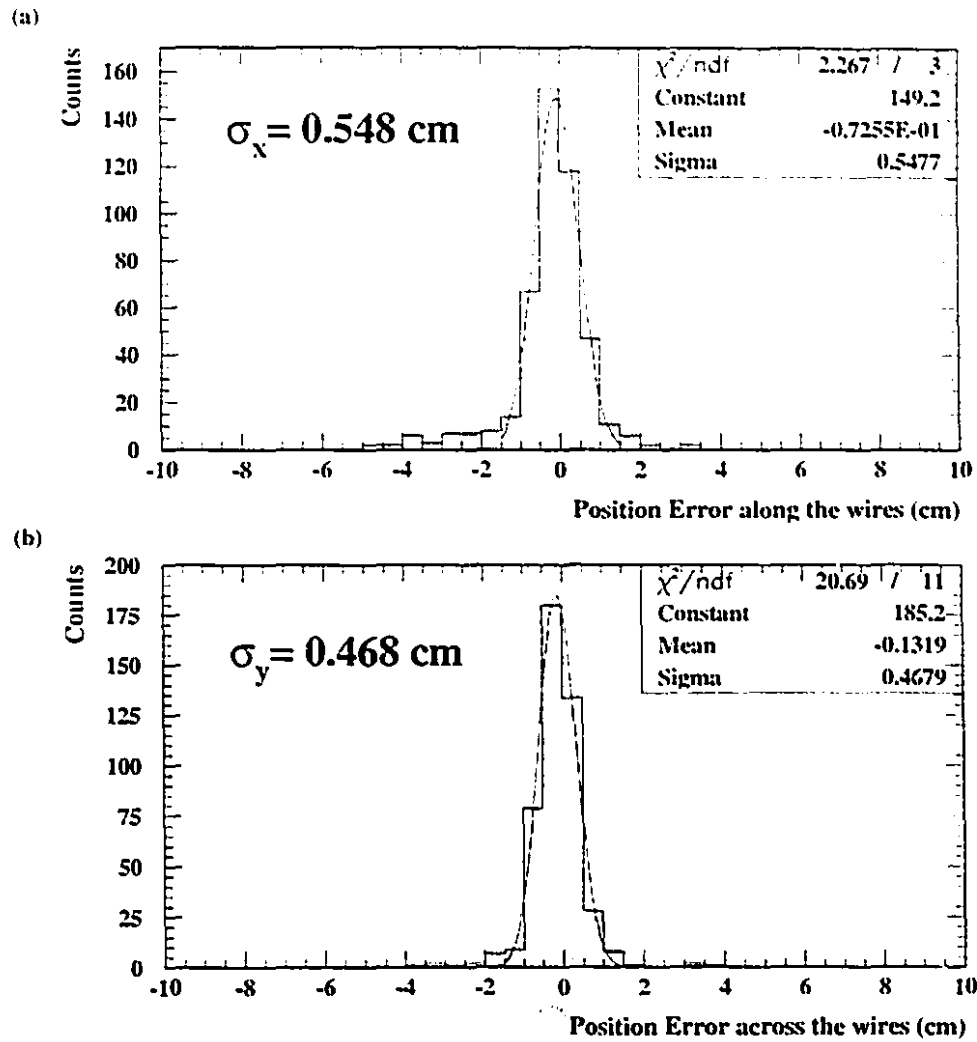


Figure 5.12: PC1 Reconstructed Position Resolution under One Particular Wire.

(a) Reconstructed Position Resolution Along the Wires; (b) Reconstructed Position Resolution Across the Wires.

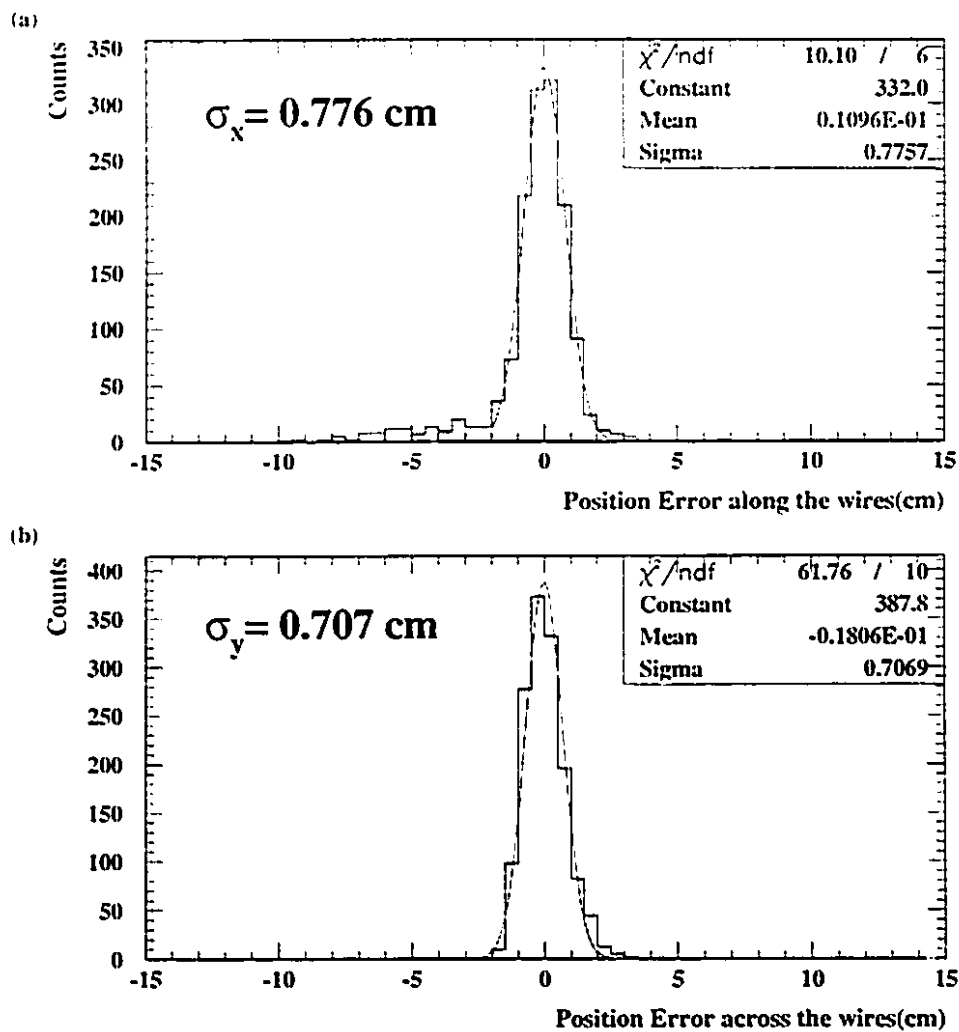


Figure 5.13: PC3 Reconstructed Position Resolution under One Particular Wire.

(a) Reconstructed Position Resolution Along the Wires; (b) Reconstructed Position Resolution Across the Wires.

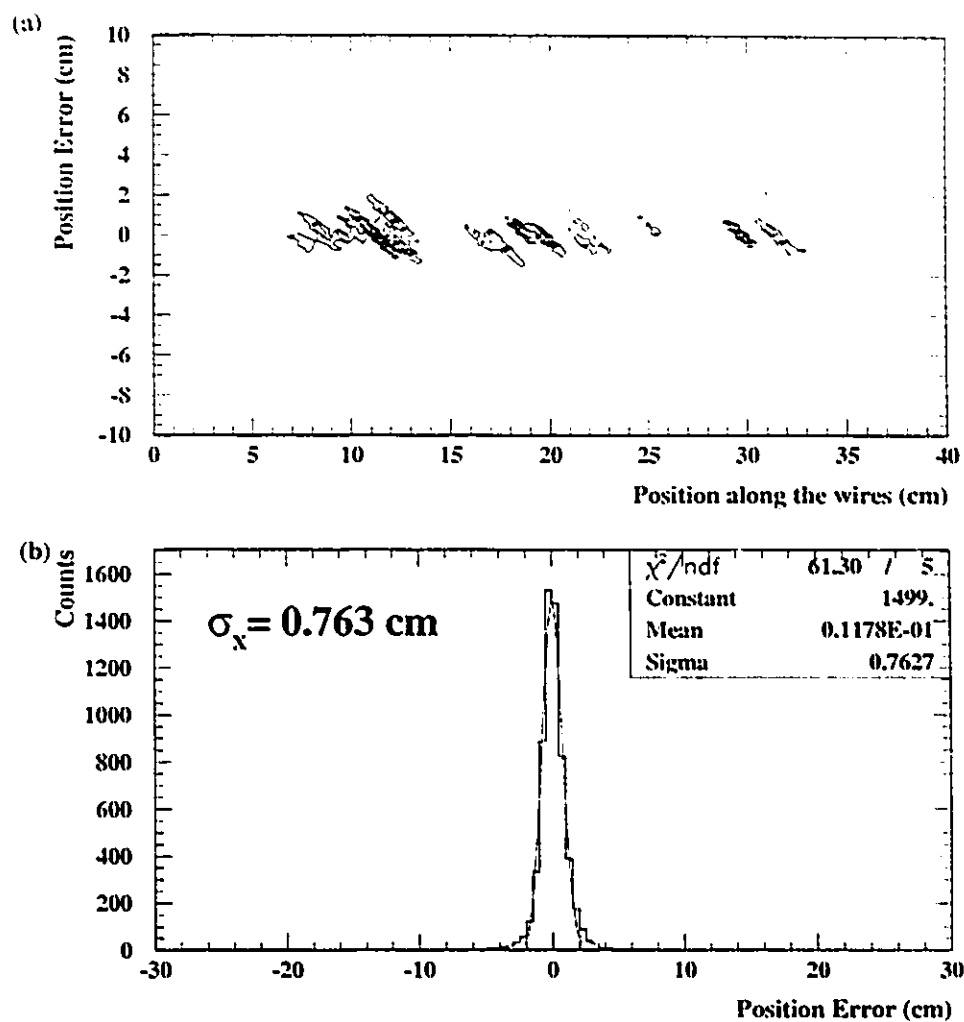


Figure 5.14: Position Linearity for PC1. (a) Non-linearity Along the Wires; (b) Global Position Resolution.

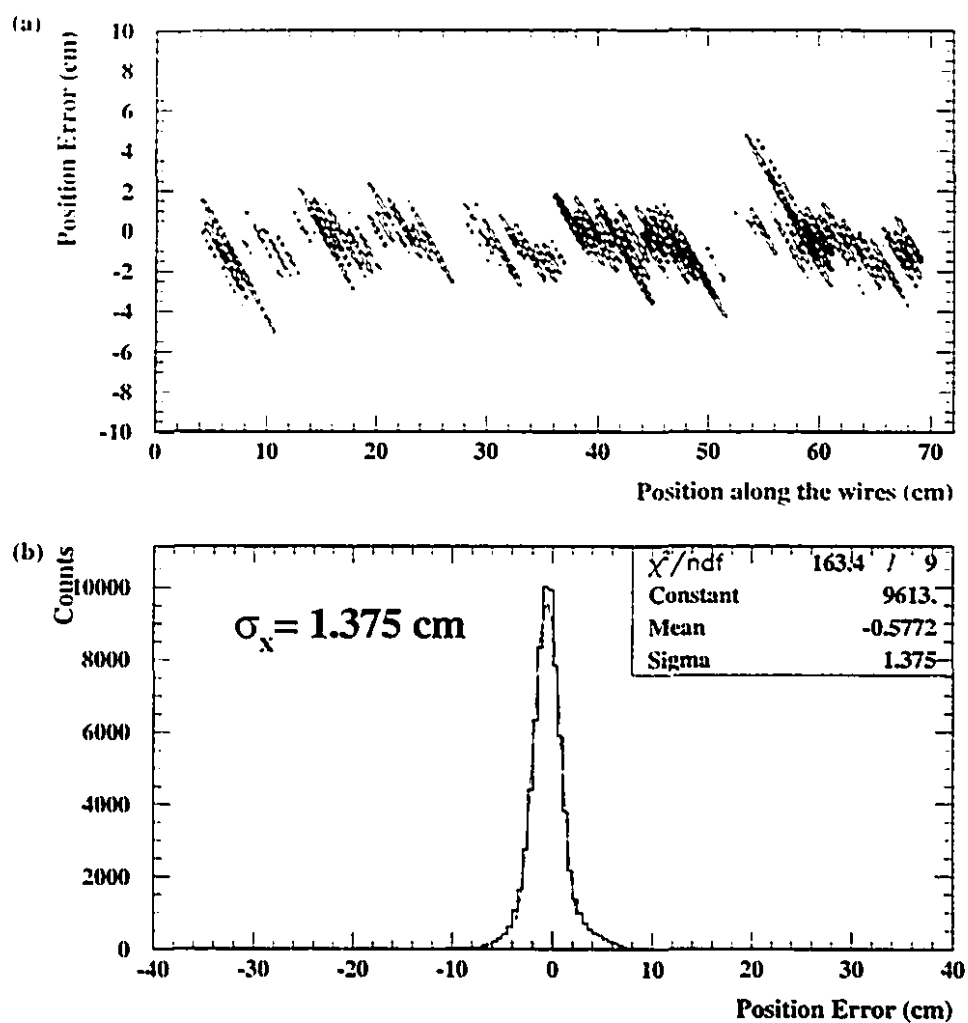


Figure 5.15: Position Linearity for PC3. (a) Non-linearity Along the Wires; (b) Global Position Resolution.

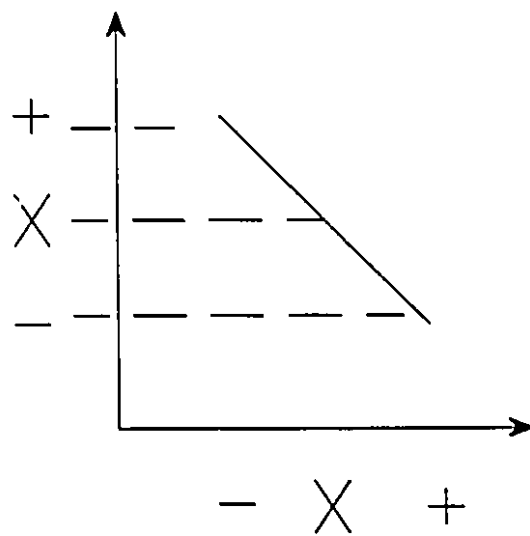


Figure 5.16: Basic Non-linearity Pattern.

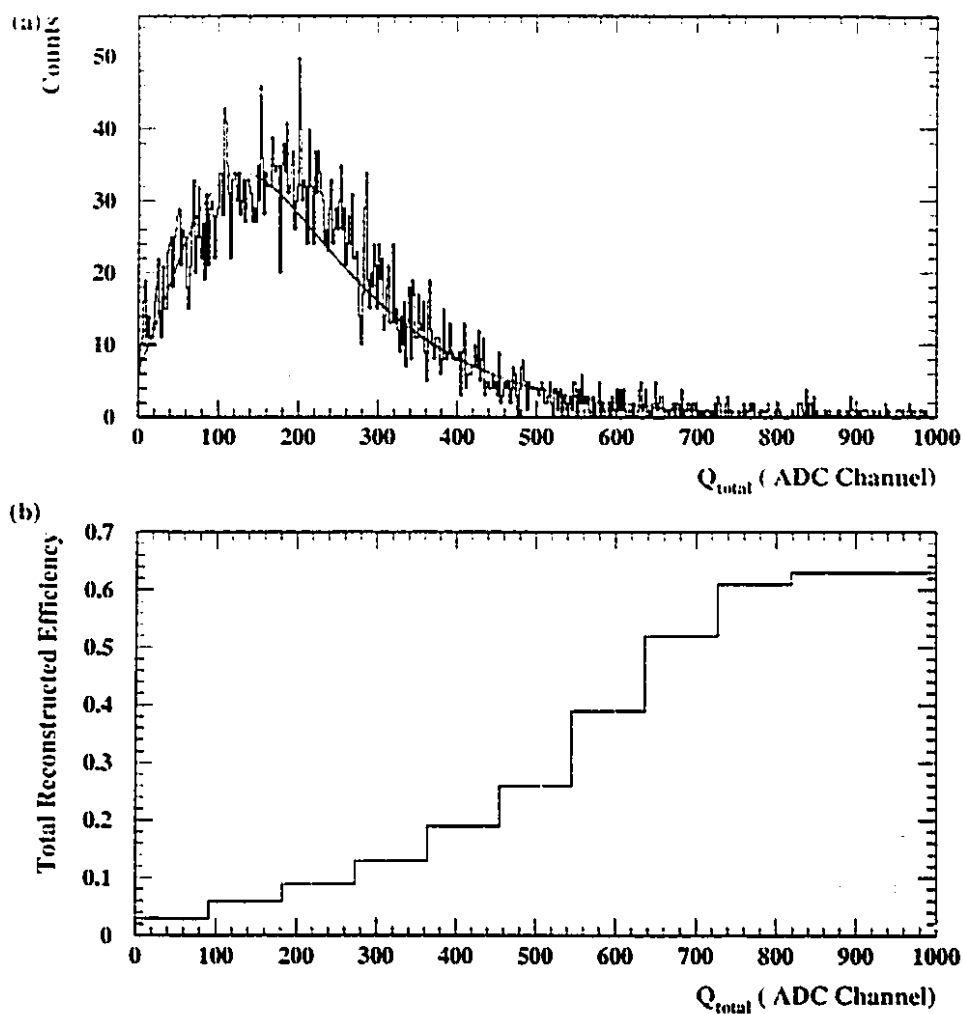


Figure 5.17: PC1, Efficiency on the Total Charge.

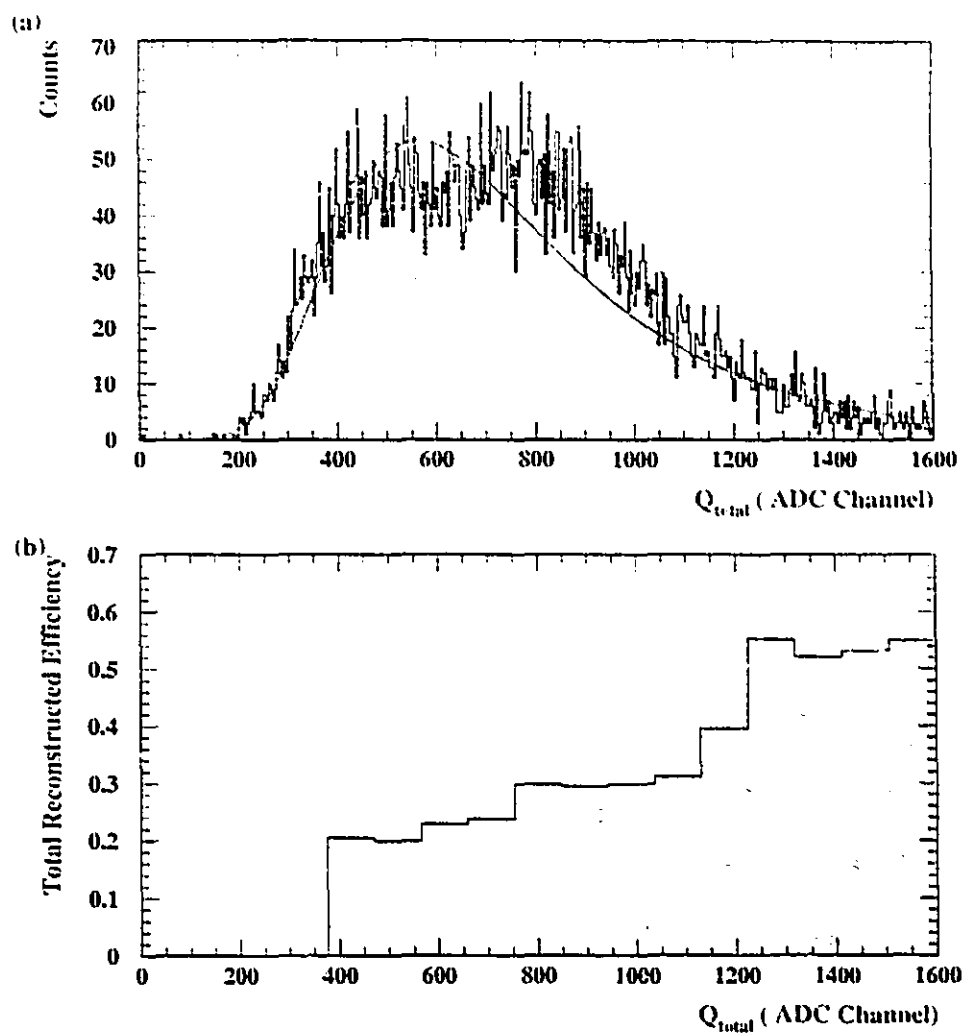


Figure 5.18: PC3, Efficiency on the Total Charge.

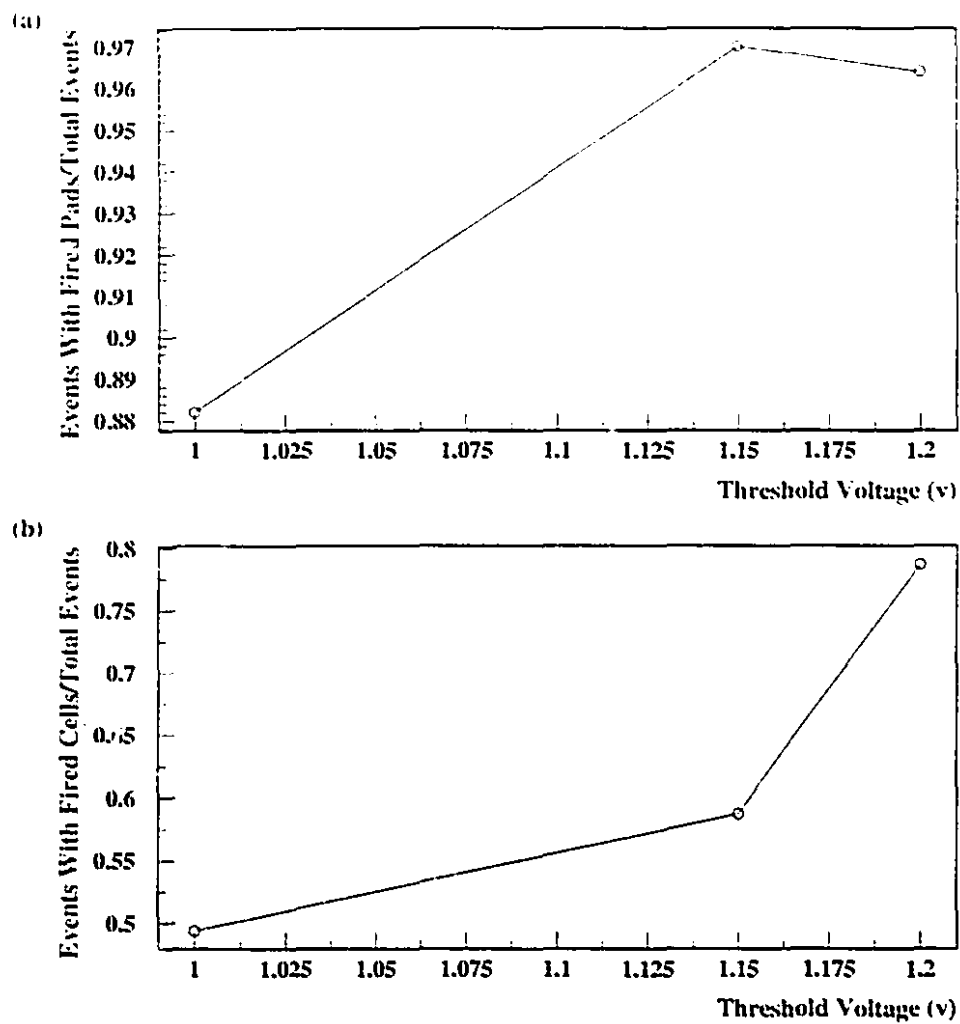


Figure 5.19: (a)Fired Pads Efficiency vs. Threshold; (b)Fired Cells Efficiency vs. Threshold.

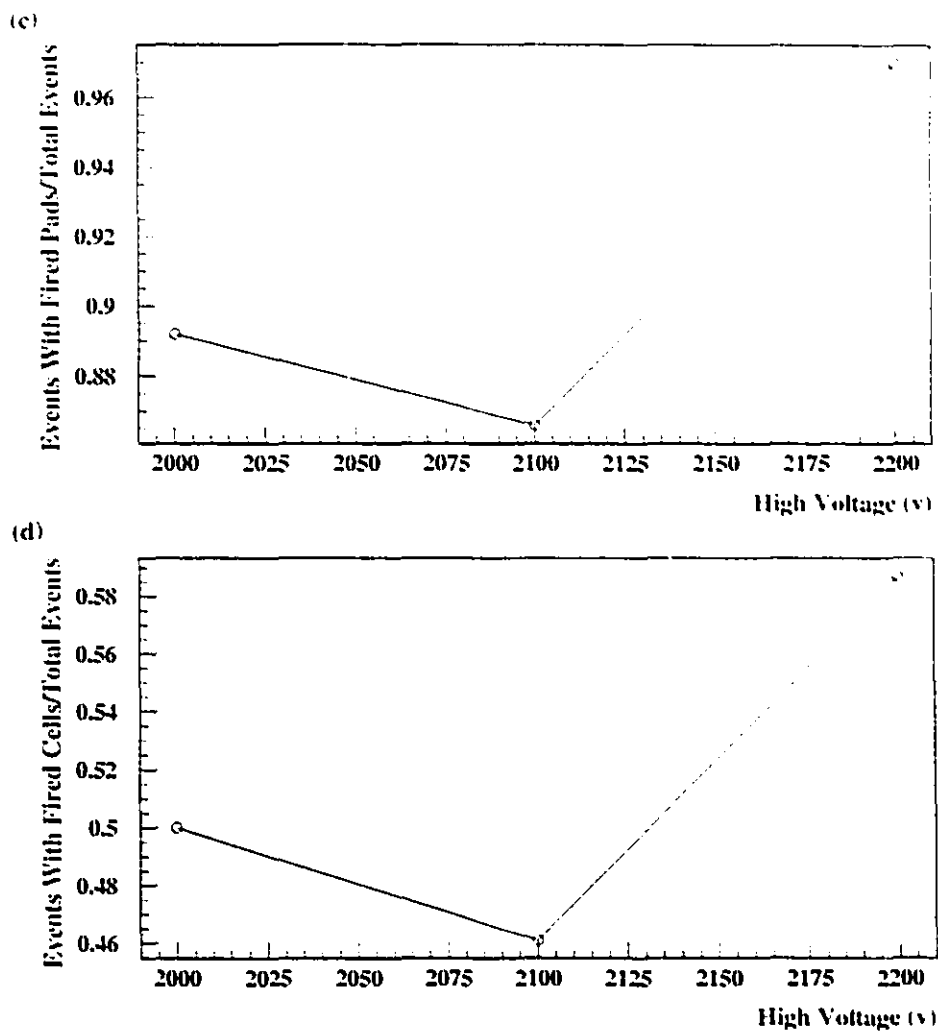


Figure 5.20: (c)Fired Pads Efficiency vs. High Voltage; (d)Fired Cells Efficiency vs. High Voltage

Chapter 6

Conclusions

6.1 Summary and Conclusions

The development of two prototype multi-wire proportional chamber (MWPC) using new pixel cathode pad readout system has been presented in the thesis. This research was conducted as part of the R&D effort on the tracking system of the PHENIX experiment at the relativistic heavy ion collider (RHIC) at Brookhaven National Laboratory (BNL).

The pad chamber is one of the PHENIX tracking subdetector systems. It is used to provide a three-dimensional position measurement to aid in pattern recognition and to determine p_z/p_T . They can also provide three space points for a second-level trigger. According to previous R&D work carried out in McGill University, the MWPC using the chevron shaped cathode for readout can offer good position resolution, low mass

and proven reliability to meet the PHENIX requirement. However, as mentioned in Chapter 2, the construction for the chevron pad chamber requires high accuracy etching for the cathode board. Also because of the requirement of relatively high precision analog readout electronics, the comparatively high cost per channel makes chevron cathode pad option less ideal than the pixel pad option. The new pixel pad chamber, using a digital readout system with highly integrated CMOS chips with the chip-on-board (COB) technology, achieved a factor of ten reduction on cost per channel. By compromising the position resolution, a pixel pad chamber could be designed and constructed with a manageable channel number by choosing the cathode pad dimension.

Two prototype pixel pad chambers, PC1 and PC3, were designed, constructed and tested in this work. The pixel pads of both the detectors were designed to have geometric size as close to as their final full scale pad chambers. The prototype PC1 has one-quarter the size of the final unit sector detector, while the prototype PC3 is approximately equal to one eighth of its final unit sector detector. The operation principles of the two pixel pad chambers were discussed in Chapter 3. Chapter 4 gave the detailed description of the detector construction and structures.

The two prototype pixel pad chambers were tested in the high energy particle beams from the Alternating Gradient Synchrotron (AGS) at BNL. A typical run without beams for PC3 was recorded for the noise study. As shown in Table. 5.1, 2.1% number of cells were found fired, triggered by all the background noise at the

experiment area at AGS. As discussed in Chapter 5.2.2, fired clusters made up with large number of fired cells were found. And according to Table. 5.2, the percentage of the missing events was comparatively high, and had strong dependence on the chamber working condition, such as discriminator thresholds, and working high voltage. As shown in Fig. 5.12 and Fig. 5.13, prototype PC1 achieved a best position resolution of $\sigma_x = 0.548cm$ and $\sigma_y = 0.468cm$, along and across the wire direction respectively, while prototype PC3 achieved $\sigma_x = 0.776cm$ and $\sigma_y = 0.707cm$. The position resolutions achieved were comparable with the one-half of their cell dimensions. Fig. 5.14 and Fig. 5.15 showed the linearity for the two chambers. If the effect of the variation in the electronics existed in these two prototypes was taken into account, they proved good linearity of the two chambers. The chambers didn't work efficiently during the tests, the reason were explained in Chap.5.2.5.

The new highly integrated CMOS chips with COB technology featured readout electronics worked very well. The uniformity of performance among different channels was proven to be critical to the chamber working performance.

This thesis has thus shown that the pixel pad chamber has good position resolution and linearity to meet the PHENIX experiment requirements. The new pixel pad readout method using CMOS chips with COB technology has dramatically reduced the cost per channel, making the relatively large channel number pixel pad chamber affordable. The chambers performance proved the feasibility and reliability of the original proposal for pad chamber in the PHENIX experiment.

6.2 Future Improvement

Some major problems were identified during the course from the in-beam tests through the data analysis. It needs possible future improvement.

1. Crosstalk due to tracks straddled more than one cell from adjacent anode wires is rather serious in both chambers, it can possibly be improved by increasing the cell spacing without increasing the number of readout channels.
2. Dead channels explain some of the inefficiency. Much more comprehensive checks are necessary during the construction period in order to avoid as much as possible dead channels.
3. Large variation in the electronics detection efficiency among channels was found. Less than 10% variation are needed for successful chamber operation.

With better understanding of the prototype pixel pad chambers, the new round of series X-ray source tests are being conducted in McGill University. The results will come after this thesis work. A full size pixel pad chamber PC1, with the identical size for the final PC1 detector is also being built here to have a in-beam test in September, 1996.

Bibliography

- [1] T. D. Lee, *Nucl. Phys.* A538, 3c(1992).
- [2] Chuan-Ming Zou, *A Measurement of Inclusive Photon Production in 10.8 A•GeV/c Au + Au Collisions*, Thesis, SUNY at Stony Brook, (1996).
- [3] J.D. Bjorken, *Phys. Rev.* D27, 140(1983).
- [4] R.Debbe et al., *IEEE Trans. Nucl. Sci.* 37, 82 (1999).
- [5] J. Fischer et al., *IEEE Trans. Nucl. Sci.* 37, 89 (1990).
- [6] Jean Barrette et al., *A Study of MWPC with Chevron Cathode Pad Readout*, *Nucl. Instr. and Meth.*, (Submitted).
- [7] The PHENIX Collaboration, *The PHENIX Conceptual Design Report*, BNL-48922, (1993), 6-22.
- [8] R. Evans, *The Atomic Nucleus*, McGraw-Hill, Inc., 1955, 581-583.
- [9] R. Veenhof, *Garfield*, a drift chamber simulation program, CERN Program Library entry W5050, (1991).

- [10] Bo Yu, *Gas Proportional Detectors with Interpolating Cathode Pad Readout for High Track Multiplicities*, Thesis, University of Pittsburgh, (1991), 13.
- [11] I. Endo et al., *Systematic Shifts of Evaluated Charge Centroid for the Cathode Readout Multiwire Proportional Chamber*, *Nucl. Instr. and Meth.*, 188(1981), 51-58.
- [12] Op. Cit. Yu, 25.
- [13] Op. Cit. Jean Barrette et al.
- [14] Op. Cit. Jean Barrette et al.
- [15] Op. Cit. Yu, 21-24.
- [16] G.C. Smith, B. Yu, J. Fisher, V. Radeka, and J.A. Harder, *Nucl. Instr. Meth. Phys. Res. A*323(1992), 78.